Sulfate mineralogy of fumaroles in the Salton Sea Geothermal Field, Imperial County, California

Paul M. Adams *, David K. Lynch, Kerry N. Buckland, Patrick D. Johnson, David M. Tratt

The Aerospace Corporation, P. O. Box 92957, Los Angeles, CA 90009, United States

A B S T R A C T

The Salton Trough lies in the transition between the San Andreas Fault and oblique spreading centers and transform faults in the Gulf of California. The Salton Sea Geothermal Field is the northernmost expression of those spreading centers. In ~2007 two ammonia-emitting fumarole fields that had been submerged beneath the Salton Sea were exposed for the first time in nearly 50 years. As the sea level continued to drop these fields have developed a number of boiling pools, mud pots, gryphons and a unique suite of ammonium sulfate minerals. These have been studied over time with long-wave infrared remote sensing coupled with ground truth surveys backed by laboratory analyses of the minerals. Many vents lie at the center of concentric rings of mineralization with systematic occurrence of different minerals from center to edge. Three semi-concentric zones (fumarole, transition and evaporite) have been defined with respect to ammonia-emitting vents and bubbling pools. The scale of these zones range from several meters, localized around individual vents, to that of the fumarole fields as a whole. The fumarole zone is closest to the vents and locally contains cavernous sulfur crystals and significant deposits of gypsum, mascagnite, boussingaultite and other ammonium sulfates. The transition zone comprises a dark brown surficial band of inconspicuous sodium nitrate underlain by anhydrite/bassanite that is thought to have formed by ammonia-oxidizing microbes interacting with the ammonium sulfates of the outer fumarole zone. The evaporite zone is the outermost and contains blödite, thenardite and glauberite, which are typical of the sulfates associated with the shoreline of the Salton Sea. Remote sensing has shown that the mineral zones have remained relatively stable from 2013 to 2017, with minor variations depending on rainfall, temperature and levels of agricultural runoff.

© 2017 Elsevier B.V. All rights reserved.

1. Introduction

The Salton Trough is a topographic low in southern California and northern Baja California, Mexico that represents a tectonically active, sedimentary pull apart basin (Lonsdale, 1989; Brothers et al., 2009; Gurbuz, 2010). Except for minor contributions from the surrounding mountains and aeolian sources, most of the sediments in the Salton Trough represent Colorado River sediments and are as thick as 6 km (Muffler and White, 1969). The trough is structurally controlled and lies in the transition between the right lateral San Andreas Fault system to the north and a series of oblique spreading centers and transform faults in the Gulf of California to the south (Macdonald, 1982). The area is dominated by a number of contiguous right lateral, right stepping (releasing) transform faults including the Imperial and Cerro Prieto faults (Meltzner et al., 2006) and those of the Sierra Cucapah in Mexico (Hauksson et al., 2011).

Within the Salton Trough lies the Salton Sea Geothermal Field where the geothermal gradient averages ~0.3 °C/m (Younker et al., 1982),

reaching a maximum of 4.3 °C/m (Lee and Cohen, 1979). About 11 commercial geothermal electricity generating plants operate in the area with a combined output of about 340 MW. The high geothermal gradient is the result of a shallow magma body from one or more spreading centers (Lachenbruch et al., 1985; Schmitt and Vazquez, 2006). Extruded magma produced the Salton Buttes, five late Quaternary rhyolitic volcanic necks near the southeastern end of the Salton Sea (Robinson et al., 1976; Newark et al., 1988). From south to north they are Obsidian Butte, Rock Hill, Red Island (north and south) and Mullet Island. The age of some of these volcanic structures has recently been dated to 2400 ybp (Schmitt et al., 2013). Recent thermal surveys have located moderate temperature (30 °C) thermal vents on Red Island north (Lynch and Adams, 2014) but the majority of higher temperature surface thermal features are concentrated southeast of Mullet Island (Lynch et al., 2013).

The Salton Sea occupies the lowest part of the Salton Trough. It is a saline, eutrophic, endorheic rift lake (Dangermond, 2003; Hurlbert, 2008) that was created when a canal breach diverted the Colorado River into the Salton Trough in March 1905 and fresh water flowed north through the New and Alamo Rivers (Kennan, 1917). After the canal was repaired in Feb 1907, the high water level of -59 m MSL decreased rapidly to around -76 m MSL in 1917. Rain and agricultural

runoff gradually raised the sea level, reaching a high of about - 70 m MSL in the mid-1980s, after which legislation resulted in a gradual lowering of the sea level that continues to this day (Lynch, 2011).

Where the Salton Sea overlaps the Salton Sea Geothermal Field, the interaction of rising gas and hot water with sea floor sediments has produced a number of fumaroles, gryphons and salses (LeConte, 1855; Veatch, 1858; Veatch, 1860; Hanks, 1882; Muffler and White, 1968; Helgeson, 1968; Sturz et al., 1992; Svensen et al., 2007, Svensen et al., 2009; Lynch and Hudnut, 2008; Onderdonk et al., 2011; Manga et al., 2009; Rudolph and Manga, 2010). Much of the activity involves rising CO_2 produced by hydrothermal alteration of calcareous components of the Colorado River sediments (Muffler and White, 1969). When bubbling water sometimes stands in the calderas of gryphons, they are termed salses. Salses are often called mud pots, and may vary in fluid content between water with small amounts of sediment to thick, viscous mud. Gryphons are relatively rare geological structures and tend to occur at active plate margins like the Salton Trough. Fumaroles, gryphons and salses with elevated temperatures often emit gasses such as CO_2, H_2O, SO_2, H_2S, NH_3, and CH_4 (Dimitrov, 2002).

The Salton Sea level began dropping about 1983, and around 2007 the fumarole fields in this study were exposed along the southeast shore for the first time since about 1945. The Salton Sea level varies seasonally in a sinusoidal fashion with a difference of about 0.35 to 0.55 m over the year with the maximum in March and the minimum in November (Fig. 1). This depends on rainfall and temperature but the Imperial Irrigation District (IID) also delivers water to the Salton Sea, and removes water from it according to their needs. Over the period of this study (2009–2017) the sea level dropped about 1.4 m. The average yearly rainfall is about 5 cm with the majority being recorded in 1–2 major events (1.5–3.5 cm) related either to late summer monsoonal or winter storms (National Weather Service, 2017).

The area to be described is an active moderate temperature (to 100 °C) ammonia-emitting and sulfate-rich fumarole area (N 33.2184, W 115.601) which has an unusual assemblage of ammonium sulfate minerals that is located 8.1 km WSW of Niland, Imperial County, California. Ammonium sulfates are uncommon and are typically associated with fumaroles (Koenig, 1969; Dunning and Cooper, 1993) or burning coal heaps (Lapham et al., 1980; Parafiniuk and Kruszewski, 2010; Masalehdani et al., 2009). There are five fumarole fields in the general area (F1–F5) (Lynch et al., 2013) and the Davis-Schrimpf fumarole field lies 3.2 km to the southeast on the same trend (Mazzini et al., 2011; Onderdonk et al., 2011). The latter field is located at the corner of

Davis and Schrimpf roads. The F1 and F2 fumarole fields (Fig. 2) are the largest and most accessible and are located on a sand spit southeast of what was Mullet Island (Lynch et al., 2014), and have been described in detail by Lynch et al. (2013). Based on historic imagery available in Google Earth, F2 was exposed sometime between August 2006 and February 2008. The area was visited by airboat on June 8, 2007 and the F2 region was found to be partially exposed. Owing to seasonal changes in Salton Sea water levels (Fig. 1), F1 and F2 have probably experienced several episodes of submersion and subaerial exposure between 2006 and 2008. Surface mud flow patterns changed markedly between the two dates. Between August 2010 and January 2011 the water level had dropped sufficiently to expose F1. In September 2011 native sulfur producing vents at F1 and F2 were confirmed for the first time. Since the vents were not noted in January 2011 it is clear that many of them surfaced during the eight month period between visits. At that time several unusual ammonium sulfates were identified, including boussingaultite and lecontite (Lynch et al., 2013). More detailed follow on field studies were conducted between October 2013 and February 2017 (Adams and Lynch, 2014). A compilation of all field visits is presented in Table 1.

There recently (2016) has been significant activity by the IID to control both irrigation runoff and more importantly windblown dust emissions. This has resulted in a significant change to the local fumarole landscape (Fig. 3). As part of a pilot project under the Salton Sea Management Program to mitigate windblown dust the IID has constructed a field of north-south oriented, 0.5 m-deep trenches, spaced about 2–3 m apart, that closely surrounds F2 on three sides and F1 on two sides. The purpose for the trenches was to trap low lying windblown sand and collect water for waterfowl habitat. Many of these trenches have acted as irrigation ditches which bring water from the marsh area to the east of the fumaroles westward and have inundated a source for windblown sand. The net result has been that while the Salton Sea level has dropped, F1 is now (based on a February 2017 visit) closely surrounded by shallow water on all sides and is difficult to approach because of very soft mud. During the spring of 2017 the 4 km trail to the fumaroles was blocked with a locked gate and "No Trespassing" signs were posted thereby restricting access. The long term existence of the fumarole field is also in jeopardy as the area has recently been leased from IID by a commercial entity as a site for a future large scale geothermal generating facility. Preliminary plans place the facility directly on top of the fumarole fields.

This study describes the sulfate mineralogy of the F1 and F2 fumarole areas in detail based on field observations from 2013 to 2017 supported with laboratory analyses of collected samples. It is coupled with long wave infrared (LWIR — nominally 7.5–13.5 μm) remote sensing studies from 2009 to 2017 which were used to map the large scale distribution of minerals over the evolution of the fumarole fields from shortly after they emerged from the Salton Sea. Ground truth surveys in 2014 and 2015 verified the remote sensing mineral identifications. There have been relatively few studies of this type which have combined extensive field collection and laboratory analysis to validate the LWIR remote sensing retrievals. Vaughan et al. (2005) performed ground truth sample collection with laboratory analyses for the Steamboat Springs, NV geothermal area. Reath and Ramsey (2013) performed a remote sensing study of the nearby Davis-Schrimpf fumarole field with limited coverage of the F2 field in this study but with limited ground truthing. This study serves as important documentation of the fumarole field mineralogy since its long term accessibility is in question as a result of dust mitigation efforts by the Imperial Irrigation District and the potential development of a large scale geothermal facility directly on the site.

2. Methods

2.1. Remote sensing

The fumarole areas have been studied by airborne LWIR hyperspectral remote sensing using the SEBASS (Hackwell et al., 1996)
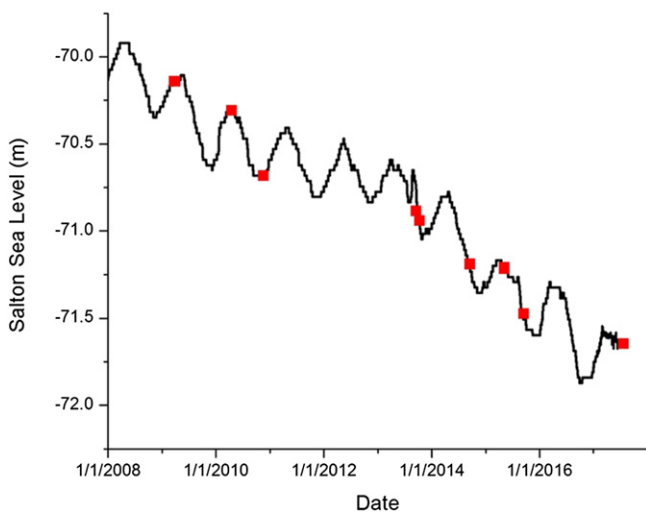

Fig. 1. Salton Sea level (above NGVD 1929) measured from the USGS Westmorland Gauging station. Larger squares are dates of remote sensing data collects. (https://waterdata.usgs.gov/nwis/dv?referred_module=sw&site_no=10254005.)

Fig. 2. Google Earth image (2015) showing the F1 and F2 fumarole fields in relation to Mullet Island (MI) and the Alamo River (AR). There is additional fumarole activity at F3 and offshore northwest of Mullet Island.

and Mako (Warren et al., 2010; Hall et al., 2011) sensors in nine data collects between 2009 and 2017 (Table 1). Mako and its predecessor SEBASS have been widely used for passive remote sensing and identification of gasses and minerals (Tratt et al., 2011; Buckland et al., 2017; Kirkland et al., 2002, 2003). SEBASS has been used in the study of other geothermal systems including the nearby Davis-Schrimpf fumarole field (Reath and Ramsey, 2013) and Steamboat Springs, Nevada (Vaughan et al., 2005). The spectroscopic observation and identification of sulfates by remote sensing is of considerable interest based on the detection of Mg and Fe sulfates on Mars (Cluotis et al., 2006; Chou et al., 2013) and the environmental consequences of acid mine runoff on Earth, which produces sulfates as a byproduct (e.g., Kim et al., 2002; McCauley et al., 2009).

These sensors operate in the nominal 7.5–13.5 μm atmospheric window. SEBASS is a nadir-viewing roll-stabilized push-broom system with an 8° swath width and 1.1-mrad instantaneous pixel field of view (IFOV), while Mako is a 3-axis stabilized whisk-broom system with a swath width programmable up to 110° and 0.55-mrad pixel IFOV. Both systems have approximately the same spectral resolution (~46 nm in 128 channels) but Mako offers superior radiometric sensitivity. The spatial resolution (ground sampling distance) of SEBASS and Mako is determined from the altitude and for these studies ranged from 0.5 m to 2 m (Table 1).

The fumarole areas were visited 19 times between 2009 and 2017 (Table 1). This included two ground truth surveys that were performed at the same time as remote sensing collects since many of the mineral growths were ephemeral and changed over time depending on rainfall, temperature, the level of the Salton Sea and agricultural irrigation runoff. An additional ground truth field operation was performed within one month of the remote data collect in 2013. Comprehensive field collects in 2013 prior to the ground truths, and subsequent mineral identifications provided the list of known minerals, from which the

eight dominant minerals were plotted in the final remote sensing mineral maps. During ground truth surveys each collection site was located using a handheld Garmin 60csx GPS receiver. The accuracy of the Garmin was on the order of ±1–2 m. As a result of the 19 field collects, over 300 samples were collected and analyzed by XRD and a similar number of Exoscan FTIR spectra were collected in the field.

The procedure for correlating remote sensing mineral maps and sample locations evolved over time since early ground truth surveys yielded equivocal results. The final method (September 2015) involved placing 25 1 m × 1 m aluminum foil (0.05 mm thick) panels around areas of interest at the margins of the various fumarole fields and near areas of mineralogical interest. This was accomplished the day before the remote data collect. Accuracy of the GPS coordinates at the Al panel end points of Exoscan traverses were ±1 m while all others were ±2 m. The bright panels are readily visible in context images taken from the aircraft with a Canon 5D Mk II camera (Fig. 4a). Between a combination of the Al panels, thermal vents and vegetation it was relatively easy to correlate field observations of mineral deposits with the context visible images, LWIR images and Tactical Analysis Report (TAR) mineral images (Fig. 4). The latter were provided to the field crew within 3 h of the flight (at the Brawley airport, BWC) and guided ground truth sampling locations for the next 1–2 days. A detailed description of the TAR is given below. The Al panels were easily discerned in the LWIR images as black "cold" pixels while thermal vents appeared light and vegetation appeared slightly darker than background. Finalized multicomponent mineral maps were typically not available until about a week after the remote collect. Larger areas (5 m²) of minerals identified in the TAR images were selected for ground truth sampling in order to maximize the chances of correct sampling considering errors in relating features in the field with context camera, LWIR and TAR mineral images. This typically limited the minerals sought in ground truth surveys to mascagnite, gypsum, nitratine and blödite, since they were the most abundant.

Table 1
Summary of field visits and remote sensing data collects.

Date	Method[a]	GSD[b] (m)	Rainfall in preceding 3 months,[c] date (m/d) (cm): daily **max/min** temperature (°C)[d]	Local time of remote collect; comments
6/24/2017	Mako	1	6/02(0.05), 5/27(0.15), 5/10(0.15): **48/26** °C	6:00 PM
2/11/2017	Field			F1 nearly surrounded by shallow water
11/25/2016	Field			Vehicular access no longer possible, dust abatement trenching completed
12/26/2015	Field			Exoscan surveys, limited dust abatement trenches present
11/26/2015	Field			Standing water returns
9/24/2015[e]	Mako/field	0.5, 1	7/20(0.28), 7/19(0.38): **42/25** °C	11:30 AM; very little standing water, mud is thick and ground dry
4/22/2015	Mako	1	3/3(0.15), 3/2(1.27), 1/30(0.08), 1/27(0.23): **28/16** °C	12:00 PM
11/27/2014	Field			Exoscan surveys
7/23/2014[e]	Mako/field	1	No rainfall: **47/28** °C	9:45 AM
1/18/2014	Field			Exoscan surveys
12/20/2013	Field			Exoscan surveys
11/6/2013[e]	Field			
10/12/2013	Field			
9/24/2013	Mako	2	9/8(0.97), 9/8(0.05), 9/5(0.33), 8/29(0.23), 8/27(0.43), 8/26(0.69): **37/18** °C	4:00 PM
8/28/2013	Mako	1	8/27(0.43), 8/26(0.69): **41/27** °C	5:00 PM
9/10/2012	Field			
2/12/2012	Field			
10/12/2011	Field			
9/15/2011	Field			Sulfur found at F1 and F2 vents
7/28/2011	Aircraft			Low altitude imaging
1/26/2011	Field			F1 exposed, lab samples collected
1/18/2011	Field			F1 exposed
11/19/2010	Aircraft			USGS Lidar study
9/18/2010	Mako	1	8/28(0.41): **42/18** °C	7:30 PM; night time remote collect
8/13/2010	Field			F2 exposed with mudflows
4/6/2010	SEBASS	1	4/2(0.18), 3/08(1.68), 2/20(0.15), 2/10(0.43), 2/7(0.53): **25/9** °C	8:40 AM; F2 exposed with mudflows
3/26/2009	SEBASS	1	2/17(0.53), 2/8(0.41): **31/13** °C	3:00 PM
7/8/2007	Airboat			F1, F2 covered with a few cm's of water
2006	Field			F1, F2 covered by Salton Sea

[a] Field collect or remote sensor
[b] Remote sensing ground sampling distance (GSD).
[c] From: www.cnrfc.noaa.gov/archivePrecipMap.php?area=rsa&month=11&day=23&year=13.
[d] At Imperial Airport; https://www.wunderground.com/history/airport/KIPL.
[e] Ground truth survey.

Details of the custom data processing developed for Mako are provided in Buckland et al. (2017). Spectral calibration is accomplished by viewing blackbody sources through a NIST SRM 1921b polystyrene film that has known absorption features and performing a least-squares fit across the entire focal plane array. Radiometric calibration, determined by observing calibrated blackbody sources at different known temperatures, is used to convert the raw instrument output to useful radiance units. Georeferencing of images is accomplished by the instrument flight software continuously recording sensor position (latitude, longitude, and altitude) from the global positioning system (GPS) and attitude (roll, pitch, and heading) from the inertial navigation system (INS) and the scan mirror encoder angles. The measured sensor radiance includes contributions from the atmospheric transmission and upwelling radiance which impose spectral features (primarily due to H_2O, CO_2, O_3, CH_4, and N_2O) onto the data. Atmospheric compensation to remove these features is accomplished through the ISAC (In-Scene
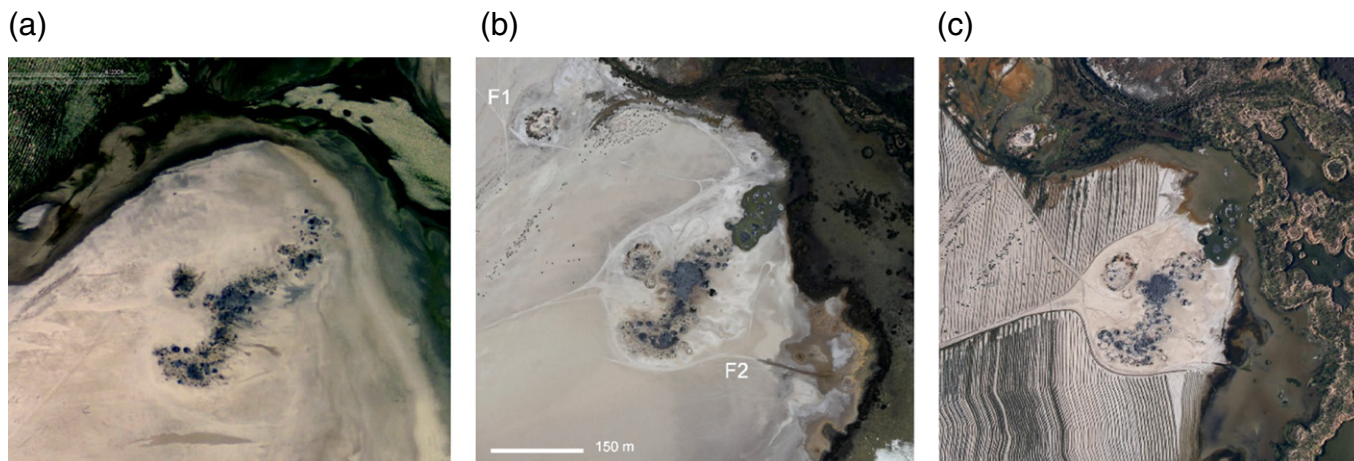

Fig. 3. Evolution of the F1 and F2 fumarole fields between 2009 and 2017. (a) Google Earth image from 2009 before the emergence of F1, (b) Context camera image, remote sensing collect April 22, 2015, (c) Context camera image, remote sensing collect June 24, 2017 after completion of the dust mitigation trenching program.
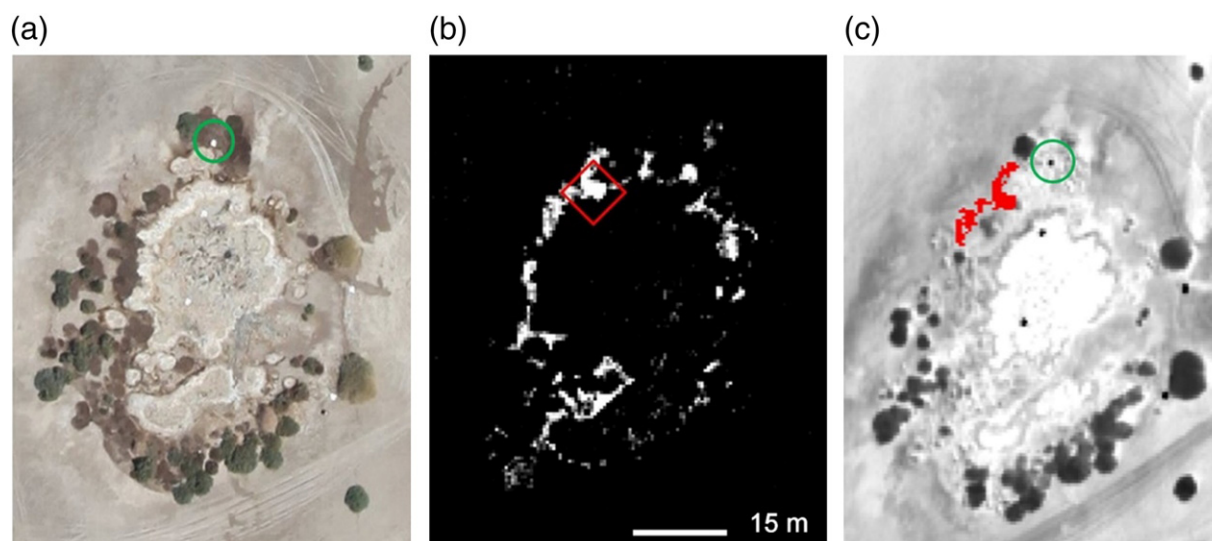
(a)　　　　　　　　(b)　　　　　　　　(c)

Fig. 4. F1 fumarole field (9/24/2015). Comparison of (a) context camera image, (b) ACE filter output (nitratine) extracted from TAR and (c) LWIR image (~11 μm) with a nitratine ROI used to locate sampling areas for ground truthing. Green circle denotes one of five 1 m × 1 m aluminum foil panels in the scene which appear bright in the context image and black in the LWIR image. Red diamond is centered on the pixel in the ROI with the greatest filter output value. The red ROI comprises connected pixels with filter output values above a specified threshold value used for ID, and in combination returned a nitratine identification in the tactical analysis.

Atmospheric Compensation) algorithm (Young et al., 2002) which makes use of the natural occurrence of blackbody (or near blackbody) surfaces within the scene (e.g., areas covered by healthy vegetation or water) and exploits the natural temperature variations over these surfaces to extract transmission and upwelling contributions directly from the measured data.

The Aerospace solids library currently in use contains 4186 reflectance signatures that have spectral features in the LWIR region and is compiled primarily from Aerospace, USGS (Clark et al., 2007), UCSB-MODIS (University of California, Santa Barbara), ASU 1.1 (Christensen et al., 2000), ASTER 2.0 (Baldridge et al., 2009), and USGS-VEG (Ribeiro da Luz and Crowley, 2010) libraries with the addition of signatures of special origin (PNNL 3.0 and NEF 9.7). The spectral library signatures are organized into family categories. The user supplies a compounds (families) of interest list (COI) and the TAR is automatically generated and subsequently updated whenever a detection and identification result contains a signature belonging to a family within this COI list. This list was based on minerals previously identified from the fumaroles (Adams and Lynch, 2014).

Solid signature variability in the LWIR is common and can be produced by variations in particle size, moisture content and aging in some cases. It is not necessary (or desirable) to produce detection filters for all of the signatures that are contained within a family. Only the spectrally unique signatures within a family are required, and the software automatically interrogates each requested family to provide a series of distinct signatures that serve as representative surrogates for the entire family. These signatures are then used to create the detection filters.

Target detection is accomplished through the use of the adaptive coherence estimator (ACE; Manolakis et al., 2003) spectral filter which provides a fast and robust method for detecting the presence of pixels with spectral similarities to known target signatures within the data with a minimal amount of user input and preparation. This filter outputs the cosine of the spectral angle in whitened space between the atmospherically compensated radiance for each pixel (after removing the scene mean vector) and the library signature under investigation. (The concept underlying data whitening in the context of hyperspectral imagery is outlined in Manolakis et al., 2003.) The whitening transformation is constructed from the full-scene covariance matrix of the data and is used to produce spectrally uncorrelated data with unit

variance across the spectral channels. In the case of the fumarole area, the spectral mean scene vector represents quartz sand and halite mixtures and the consequence of the mean scene removal process means that quartz/halite cannot be identified/mapped.

Each of the spectral filter output images (ACE) are automatically assessed for the presence of target signatures by requiring that the filter output values exceed some predefined threshold value within a specified region of pixel connectivity. These region of interest (ROI) specifications are each encoded with the location (pixel coordinates, latitude and longitude) corresponding to the pixel with the largest magnitude of filter output within the ROI, the number of pixels contained within the ROI and the mean spectrum of the ROI pixels. The mean spectrum of each ROI is then passed to the identification stage for further processing. Until this final step the ACE images only represent regions with spectral similarities to the signatures used to create the various filters.

The goal of target identification is to uniquely determine the composition of the mean spectral vector for each ROI, using a library of possible reference spectral signatures. This is done by applying the *stepwise* generalized least-squares (GLS) algorithm (Draper and Smith, 1998) coupled with a large spectral library database that currently contains 4186 solid signatures. Once the ID is complete, a tactical analysis report (TAR) entry is generated and subsequently updated whenever the ID results contain a requested compound (signature) included within the COI list. These TAR entries display an ACE filter output as gray-scale using a specified linear stretch with red-diamond target designator overlaid (Fig. 4b), and a ROI image that shows the pixels selected for ID superimposed in red onto the thermal image (~11 μm, Fig. 4c). A real-space representation of the spectral fit using the combination of signatures that were identified in whitened-space is also returned by the ID algorithm (e.g., Fig. 5). The TAR report contains the sum of the entries for all the ROIs for each mineral for each whisk. For scattered mineral occurrences with poor connectivity there may be a considerable number of ROIs and TAR entries for each mineral.

Examples for a nitratine TAR entry at F1 are given in Fig. 4 where the red diamond is centered on the pixel in the ROI with the greatest ACE filter output value (highest spectral correlation to signature). The ACE filter output images are displayed using a linear stretch of 2σ to 6σ which translates to brightness of the pixels corresponding directly to filter output strength in this range. The red ROI comprises connected pixels with filter outputs exceeding a specified threshold value. The
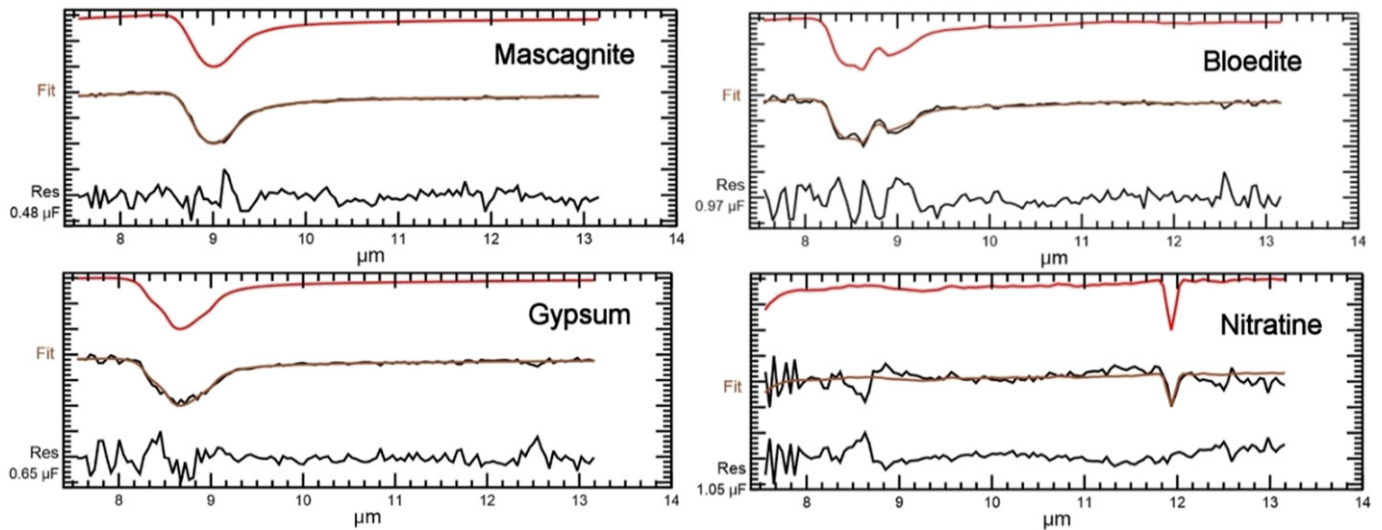
Fig. 5. Example comparisons of library reference spectra (top), real-space representation of the spectral fit using the combination of signatures that were identified in whitened-space (middle) and the spectral residuals (with RMS value) of the spectral fit (bottom). The scale of the spectral residual has been expanded to show detail. From the 9/24/2015 Mako data collect.

mean spectrum of these ROI pixels returned a nitratine identification in the tactical analysis.

Fig. 5 shows examples of library reference spectra along with a real-space representation of the spectral fit using the combination of signatures that were identified in whitened-space. The middle plot displays the atmospherically corrected (minus background and mean scene vector) ROI spectrum superimposed with the best spectral fit from the library. The spectral residuals (with RMS value) of the spectral fit are also shown with the scale expanded to show detail.

The SEBASS/Mako GSD (ground sample distance) ranged from 0.5 to 2 m depending on altitude. Therefore in most cases the measured radiance was integrated over regions containing a variety of surface materials, often significantly so. The ID algorithm is capable of returning up to 10 compounds from the library through linear unmixing in whitened space (if necessary) to successfully fit the data of mixed pixels.

Large scale false-color multi-mineral maps compiled from georeferenced whisk mosaics are created by following a similar procedure with the ID done on each pixel (rather than selected ROI's). These maps are generated by ignoring all but the dominant spectral (not spatial)

component. Typically about 8 minerals are mapped so that individual colors (minerals) can be easily discriminated. The generation of these maps was more time consuming since an identification must be performed for each pixel rather than the individual ROIs in the TAR, and this process was not generally completed until about a week after the data collect. Estimation of pixel fill fraction is generally not possible since many of the spectra in the solids spectral library are not calibrated for absolute measurements.

2.2. Laboratory and field studies

Mineral identifications were made using powder X-ray diffraction (XRD), coupled with energy dispersive X-ray spectroscopy (EDS) in the scanning electron microscope (SEM). XRD was performed with a PANalytical X'Pert Pro diffractometer using copper radiation. A small amount of material (typically 0.05 g) was scraped from the surface and ground in a mortar and pestle and pressed against a zero background plate (quartz crystal cut so as to produce no XRD reflections). In the scraping process it was common to incorporate some underlying material (typically quartz sand). Most samples were analyzed in θ–2θ
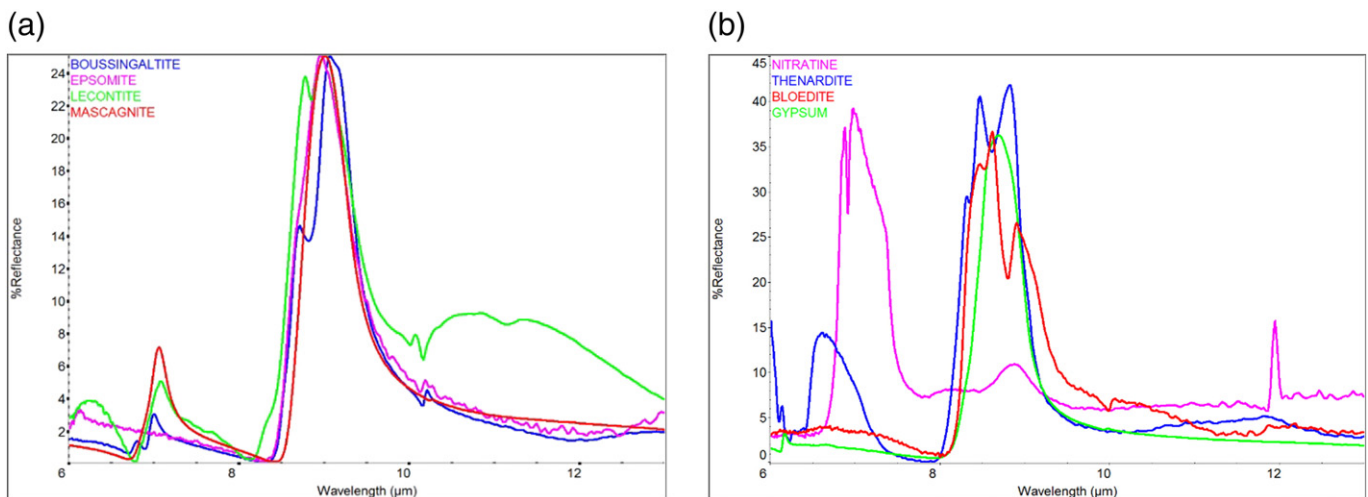

Fig. 6. Comparison of biconical reflectance spectra of minerals from the fumarole fields. Spectra scaled for better comparison. (a) Boussingaultite, mascagnite, lecontite, and epsomite. (b) Nitratine, blödite, gypsum and thenardite.
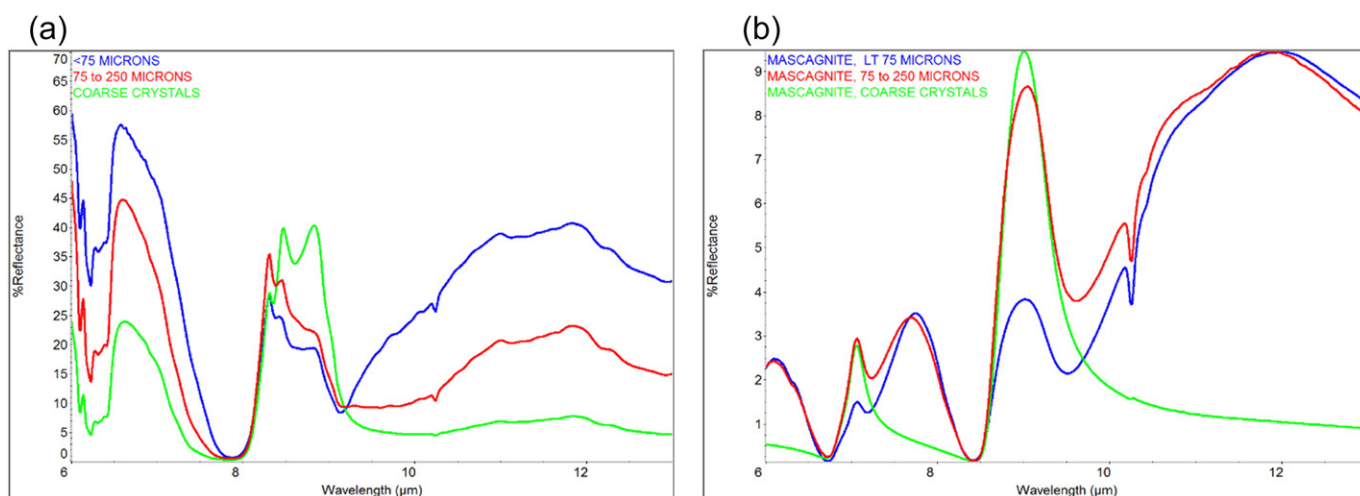
(a)

(b)

Fig. 7. Comparison of biconical reflectance spectra as a function of particle size. (a) reagent sodium sulfate (thenardie). (b) reagent ammonium sulfate (mascagnite).

mode with an X'Celerator strip detector for quick analysis. Selected surfaces were analyzed directly with parallel beam optics (X-ray mirror and parallel plate collimator). This method was more surface sensitive (10s of μm) with less chance of incorporating underlying material but was more time consuming. It can also analyze irregular surfaces without introducing peak shifts or peak broadening from sample topography and displacement. Interpretation is more complicated as a result of fewer crystallites being present and the likelihood of preferential mineral growth directions, both of which produce different relative peak intensities compared to reference patterns.

SEM/EDS was performed with a JEOL model 6460LV variable pressure SEM (base pressure 35 Pa) equipped with an Oxford Xtreme EDS operated with INCA software. Cross sections of selected samples were prepared for SEM/EDS analysis in order to better understand mineral distribution as a function of depth. After pulling a vacuum to evaporate any remaining fluid, samples were potted and impregnated with epoxy. They were then sectioned dry with a band saw and ground and polished (120–1200 grit SiC) using mineral oil so as not to dissolve water soluble phases. The oil residue was removed with methanol and the samples were carbon coated to prevent charging in the SEM.

Laboratory Fourier transform infrared (FTIR) measurements were made at 4 cm^{-1} resolution with a dry nitrogen purged Thermo Nicolet model 6700 FTIR spectrometer equipped with DTGS and MCT-A detectors. Biconical diffuse reflectance measurements were performed using a Harrick "praying mantis" accessory. Labsphere Infragold was used as the background reference. Biconical reflectance (R) spectra can be related to remotely collected emissivity (ε) spectra by Kirchhoff's Law ($\varepsilon = 1 - R$) (Hunt and Vincent, 1968; Salisbury et al., 1994). Such measurements reproduce spectral shapes accurately but are not quantitative. Reference spectra were measured from selected samples identified by XRD as relatively pure materials. These reference spectra were added to the Aerospace Solids spectral library. Limited attenuated total reflectance (ATR) analyses were made with a Durascope single-bounce diamond ATR accessory. Laboratory measurements were ideally made within one week of field collects in order to minimize changes to the samples resulting from desiccation or subsurface fluids wicking to the surface by capillary action and dissolving existing species or precipitating new minerals.

An Agilent Technologies model 4100 Exoscan portable FTIR was used to make selected diffuse reflectance measurements. In the field the Exoscan was interfaced with a personal computer (PC) for data collection with both located under large umbrellas to provide cooling shade (daytime highs to 45 °C) and to make the PC screen visible in

otherwise bright sunlight. Field samples typically had very rough surfaces which required the use of the 100 μm diffuse standard and maximum gain settings on the Exoscan in order to record spectra. Concentric mineral growths are commonly observed around thermal vents. In order to better understand these, sampling "traverses" were conducted and specimens were analyzed using the Exoscan. The traverses were oriented radially from the central vent and across mineral zones. Each traverse was marked with stakes beginning as close to a central sulfur producing vent or bubbling pool as possible and ending in sand/halite where there was no obvious mineral growth of interest. The locations of the stakes were recorded with GPS. A tape measure between the stakes was used to record the locations of samples which were collected and returned to the Exoscan for immediate analysis. This aided in the selection of material to be returned to the lab for further XRD analyses. Generally only those samples that produced a significant sulfate signature were considered for further XRD analysis since many of the minerals of interest mapped by airborne LWIR remote sensing were sulfates. During later ground truth surveys the ending traverse location was also marked with an aluminum foil panel which could be readily located in the airborne LWIR images. The Exoscan diamond ATR attachment, which produces transmission-like spectra, was also used to make selected mineral identifications in the field.

Fig. 8. F1 fumarole field from 8 m elevation looking south towards Red Island (11/26/15). Note vehicle for scale and steam from boiling pools and zoned mineralized satellite vents.
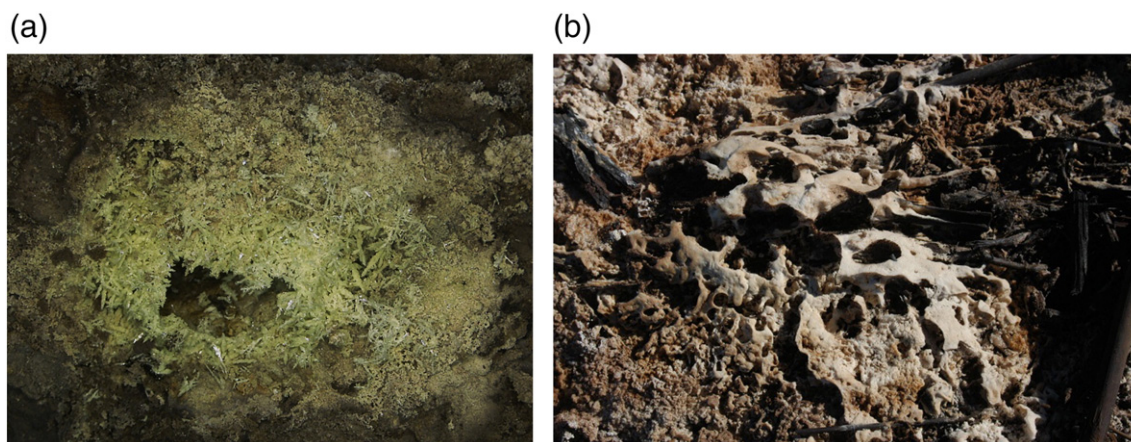
Fig. 9. (a) Sulfur producing vent at F1. Field of view is 8 cm. (b) Mascagnite growth on dead vegetation near a vent at F1. Field of view is 30 cm.

3. Infrared spectroscopy of sulfates

Sulfates, which are common at the fumarole fields, have characteristic absorption bands between 8.5 μm and 9.5 μm in the infrared that are attributable to v_3 S-O bending and v_1 S-O stretching (Cluotis et al., 2006; Lane, 2007). In diffuse reflectance (DR) spectra they appear as reflectance maxima (reststrahlen bands). Reference DR spectra were measured from selected samples identified by XRD to be relatively pure materials. Fig. 6 shows examples of representative spectra used for screening samples for further investigation. These reference spectra were subsequently added to the Aerospace Solids Library. The sulfate spectra are all very similar but show slight wavelength shifts and distinctive lobes and shoulders that can be used in identification. Boussingaultite, lecontite, mascagnite and epsomite have reflectance maxima from 9.07 μm to 8.96 μm, respectively, in descending order. Lecontite and boussingaultite can be distinguished by their subsidiary maxima at 8.78 μm and 8.71 μm, respectively. The nitrate band at 12 μm in the nitratine spectrum is distinctive along with the complex band at 7 μm, the latter of which cannot be observed in remote sensing spectra because it is outside the atmospheric window.

Reflectance spectra show variations which are dependent on particle size or surface roughness as the contribution from volume scattering over surface scattering increases with decreasing particle size (Hunt and Vincent, 1968; Salisbury and Wald, 1992; Mustard and Hays, 1997). Examples are shown in Fig. 7. In general, spectral contrast decreases with decreasing particle size and the intensity from the broad transparency feature at longer wavelength increases with respect to the reststrahlen band (Salisbury and Wald, 1992). This complicates remote sensing identifications since multiple spectra for individual minerals must be present in spectral libraries in order to cover a range of particle sizes. It was not possible to obtain fine grained (<75 μm)

reference spectra for many of the fumarole sulfates and the only library spectrum for lecontite (Fig. 6a) most likely represents fine grained material based on the strong reflectance transparency feature at 11 μm.

4. Fumarole field mineralogy

4.1. Overview

F1, the westernmost fumarole field, is about 650 m SE of what was Mullet Island (Lynch et al., 2013) and 400 m NW of F2 (Figs. 2, 8). It is elliptical, about 25 m × 50 m, and has abundant small clear to thin muddy boiling pools, sulfur producing vents and associated sulfate accumulations (Fig. 9a, b). It has no elevated structures (gryphons) (Fig. 8). The subsurface generally consists of dark gray to black mud, sand and locally has hard deposits of cemented small pelecypod shells and remnants of plant stems. Unlike F2, F1 is surrounded by vegetation, predominantly iodine bush (*Allenrolfea occidentalis*). Living plants are in close proximity to the fumaroles and dead plant material is common and often mixed in with the mud and ammonium sulfates (Fig. 9b). Water temperatures were typically boiling (100 °C) and the total dissolved solids were 3 g/l compared with 48 g/l for Salton Sea water (Table 2).

The F2 field is roughly 120 m × 400 m and irregular in shape. It is subdivided into the F2 north complex (F2NC), a small outlier to the northwest and the F2 base complex (F2BC). Fluids at F2 are more viscous than at F1 which has allowed the development of hundreds of mud pots and gryphons to 1.5 m high, though the height varies with time and seasonal ground-water levels (Fig. 10a). Their base diameters varied from a few cm to up to 10 m. Some are single structures, others are composites of several gryphons that grew and merged together. F2 also contains hundreds of "mud towers", which consist of slender vertical tubes with central vents emitting hot gas and relatively thin mud (Lynch et al., 2013) (Fig. 10b). They ranged in height from a few cm to over 0.5 m, and were between 3 cm and 20 cm wide. Isolated mud towers were the most common, but many were also formed inside or atop composite gryphons. Water temperatures ranged from boiling to ambient for areas of some larger pools on the eastern margin of the field.

Laboratory analysis revealed that the main component of the mud from the gryphons was quartz (~60–80%). Gypsum, halite, calcite, dolomite and various minor feldspars were also present. Despite the variation in mud color, there was little if any difference in composition. A number of common sulfate minerals, including glauberite, bassanite, anhydrite, thenardite, and blödite, were present in minor amounts. The minerals found at F1 and F2 are similar. Ammonium sulfates are present at both fields but are much more common at F1. Sulfur producing vents and living and dead vegetation are more common at F1,

Table 2
Total dissolved solids (TDS) content in pools from F1 and F2.

Location	Sample	TDS (g/l)	Residue determined by XRD
F1	A	3	GYPSUM, Halite, Sal ammoniac, lecontite, boussingaultite
F1	B	3	HALITE, Gypsum, lecontite, boussingaultite, sal ammoniac
F2	WP303	3	HALITE, Sal ammoniac, Gypsum, lecontite
F2	WP450	3	GYPSUM, Mascagnite, boussingaultite, lecontite
F2	WP451	34	HALITE, gypsum, sal ammoniac, sylvite, calcite?
F2	N Pool	87	HALITE, gypsum, unknown?
F2	SE Pool	3	HALITE, Gypsum, Sal ammoniac, boussingaultite
Salton Sea		48	HALITE, gypsum, blödite, hexahydrite

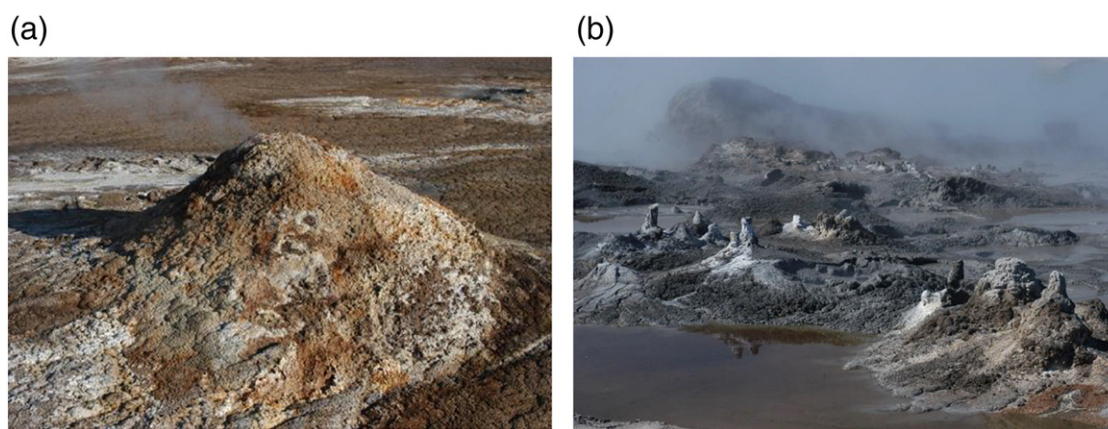Abundance: MAJOR, Minor, trace.

(a)

(b)

Fig. 10. (a) Sulfate encrusted gryphon (1 m high) from west side of F2 base complex fumarole field. (b) Field of mud towers from the southeast side of F2. Height of tubes is about 20 cm.

compared with F2. The fumaroles at F1 are less extensive but were more accessible than F2. Brown rings containing nitratine and anhydrite typically form around the ammonium sulfates at both F1 and F2 (Fig. 11).

Plumes of ammonia gas have been observed emerging from the F1 and F2 fields (Tratt et al., 2011, 2016) and are thought to produce the ammonium sulfates. The source of the ammonia had originally been assumed to originate from thermal decomposition of plant matter or fertilizer residues from agricultural runoff (Tratt et al., 2011 and references therein). However, it is noted that elevated levels of dissolved ammonia have been measured in the deep seated hypersaline brines beneath the region (Bishop and Bricarello, 1978; McKibben, 2008) and that ammonium salts were suspected far earlier than agricultural development (LeConte, 1855). Ammonia has not been detected from the nearby Davis-Schrimpf fumarole fields (Mazzini et al., 2011) but emissions of ammonia from the cooling towers of the associated Energy Sources Featherstone geothermal plant point to a more deep seated origin (Tratt et al., 2016). Ammonium sulfates have been found at other fumarole fields where irrigation and agricultural runoff are not a potential source of ammonia. This includes ammonioalunite, ammoniojarosite, boussingaultite, letovicite, mascagnite, and tschermigite from the Geysers in Sonoma County, CA (Dunning and Cooper, 1993; Koenig, 1969); tschermigite and boussingaultite from a geyser in Peru (Ciesielczuk et al., 2013) and boussingaultite from Coso Hot Springs, Inyo County, CA (Ross and Yates, 1942). A suite of rare ammonium-containing minerals have also been found at La Fossa crater, Vulcano, Sicily (DeMartin et al., 2009). Ammonium-bearing feldspar and alunite have been observed at gold- and mercury-bearing hot springs deposits in Nevada, and California, as well as at several other hydrothermal

systems in the western United States (Krohn et al., 1993). Ammonium sulfates are also commonly associated with exhalations from underground coal fires (Lapham et al., 1980; Parafiniuk and Kruszewski, 2010; Masalehdani et al., 2009).

The pH of the water in the bubbling and boiling pools (measured with colorpHast pH strips) is nominally neutral (6.5–7.5). The pH of pools at the nearby Davis-Schrimpf fumarole field, which were measured more accurately with a digital pH meter, ranged from 5.2 to 6.8 (Svensen et al., 2007, 2009; Mazzini et al., 2011). The total dissolved solids in 2 clear pools at F1 was 3 g/l and 5 clear to milky pools at F2 ranged from 3 to 87 g/l compared with 48 g/l for Salton Sea water (Table 2). Residues remaining after evaporation consist primarily of halite though gypsum was the main constituent of two pools. Minor to trace amounts of ammonium salts, such as sal ammoniac, lecontite, mascagnite and boussingaultite occur in some residues. The major residue from Salton Sea water is halite with trace amounts of gypsum, blödite and hexahydrite. It is interesting to note that mascagnite was not more common in the residues from the fumarole water considering how prevalent it is surrounding the pools and vents. As a result, it is clear that the extensive ammonium sulfate salts do not form from the simple evaporation of the water from the bubbling and boiling pools. Instead it is conjectured that ammonia and SO_2/H_2S percolating through the wet sand and mud near gas vents react to form ammonium sulfate solutions that are concentrated and then brought to the surface by capillary action to form the efflorescent growths (Fig. 9b). In fact, ammonia has been suggested as an effective agent for scrubbing SO_2 from the stacks of coal fired power plants (Shale, 1974).

4.2. Remote sensing results

4.2.1. Overview

The context camera image of the F1 and F2 fumarole fields from July 2014 is shown in Fig. 12a along with the brightness temperature image (Fig. 12b) computed from the radiance data. Temperatures >60 °C were recorded from a large area located in the center of F2. This corresponds with an area of bubbling mud (Fig. 13). Temperatures of up to 100 °C have been measured on the ground from selected mud pots and clear boiling pools at F1 and F2. A map of ammonia emissions is presented in Fig. 14a and shows four major sources. The ammonia abundances were determined by the procedure described in Buckland et al. (2017). The prevailing wind direction was to the SE so the sources of the plumes are at the western most points. The largest plume is correlated with the large high-temperature bubbling mud pot field in F2 (Fig. 13) which is relatively devoid of sulfate mineralization. Other significant ammonia emissions are located at F1, F2NC and F2BC. Fig. 14b is a map showing the eight most common sulfate minerals associated with the F1 and F2 fumarole fields superimposed on the thermal radiance image for reference. Only the dominant mineral in each pixel is plotted. This map was
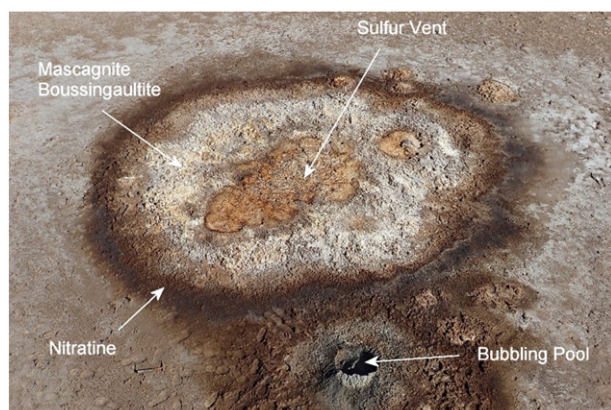

Fig. 11. Satellite vent at F2 showing mineral zonation from 6 m elevation. Field of view is 4 m. White areas and brown rings contain ammonium sulfates and nitratine, respectively.
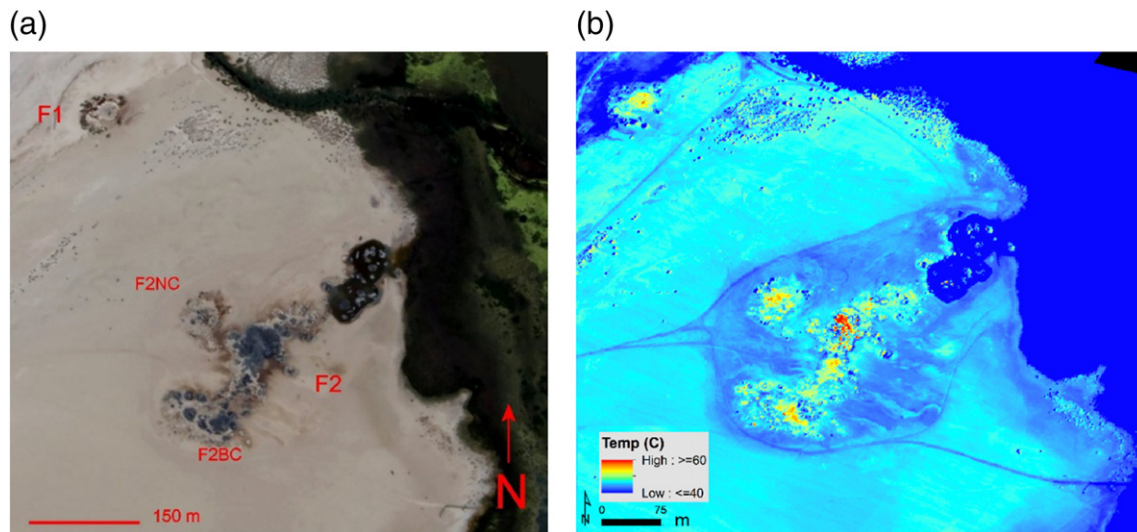
(a)

(b)

Fig. 12. (a) Context camera image of the fumarole fields on 7/23/2014. (b) Brightness temperature image of the F1 and F2 fumarole fields (7/23/2014).

created by combining 9 whisks. The sulfate minerals are not only associated with the areas of ammonia discharge in the F1 and F2 fumaroles but also occur along the brush/shore line bordering the marsh at the right of the image. A map of ten other sulfate minerals, including: alum-(Na), alunite, bassanite, glauberite, gwihabaite (ammonium nitrate) lecontite, mirabilite, sal ammoniac, sodium alum, tschermigite and urea was also generated. These other minerals, when present, generally only represented a few pixels and were difficult to locate and verify by ground truth.

Fig. 15 compares a more detailed view of the sulfate mineral map for F1 compared with the ammonia plume. The plume originates from a small area of boiling pools in the center of an area of gypsum but the ammonium sulfate and nitrate mineralization has developed a series of concentric zones a considerable distance ($\sim$20–30 m) from the greatest ammonia emissions.

An enlarged view of the mineral map showing the F2NC field along with the context camera image from September 24, 2015 are shown in Fig. 16. Darker rounded features which are not mapped as minerals are clumps of vegetation. At F2NC the minerals tend to define a series of somewhat concentric rings. Mascagnite [$(NH_4)_2SO_4$] and boussingaultite [$(NH_4)_2Mg(SO_4)_2\cdot 6H_2O$] are found near the center, closest to the area of ammonia emission. These are followed outwardly by gypsum

[$CaSO_4\cdot 2H_2O$], nitratine [$NaNO_3$] and blödite [$Na_2Mg(SO_4)_2\cdot 4H_2O$]. The blödite is more concentrated on the west side of the field while the nitratine is developed preferentially on the east side. Halite is usually found beyond the blödite ring but it does not have a LWIR signature that can be mapped (for a more detailed discussion of the spectral signature associated with halite areas see Section 4.2.4). There is a similar nearly concentric zonation of minerals at F1 (Fig. 15) except that the order of gypsum and mascagnite zones is reversed and the nitratine ring is incomplete. Based on these results and field observations the mineralization is divided into three roughly concentric zones. Outwardly from the central boiling pools and fumarole vents the zones are: fumarole, transition and evaporite. For the purposes of the remote sensing mineral maps the dominant minerals in each zone are (in parentheses): fumarole (mascagnite, boussingaultite and gypsum), transition (nitratine) and evaporite (blödite and thenardite). More detailed descriptions of the minerals in each of the zones are described in Section 5.

4.2.2. Ground truth results

Fig. 16 shows locations at F2NC where ground truth sampling was performed. Way points (WPs) in Fig. 16a can be related to samples identified in the laboratory by XRD (Table 3) and additional ground truth results for F2BC are presented in Table 4. The X's in Fig. 16b note locations

Fig. 13. Large field of boiling mud pots at the center of the F2 fumarole field.
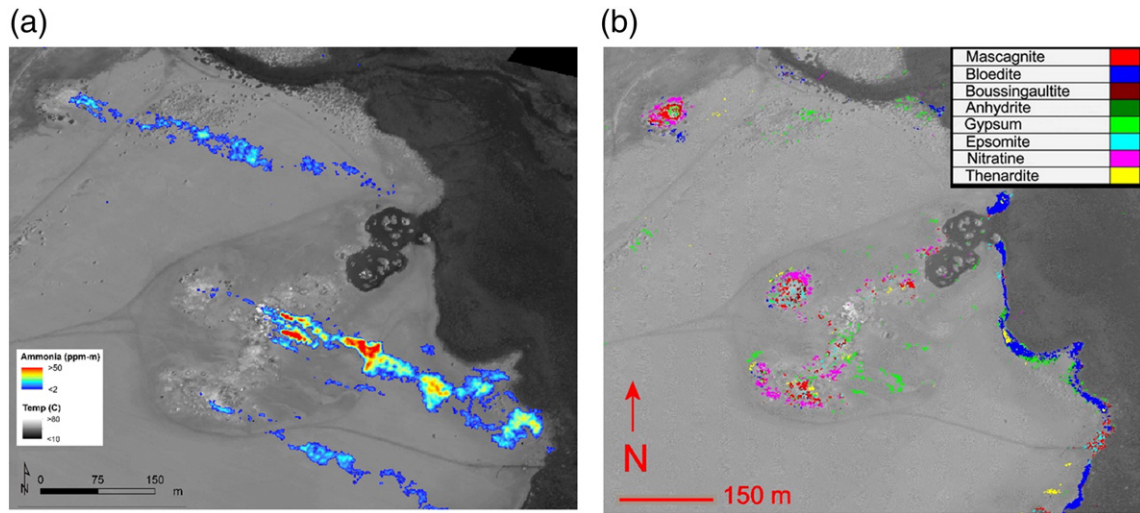
Fig. 14. (a) LWIR hyperspectral false color ammonia column density at the F1 and F2 fumarole fields superimposed on gray scale surface brightness temperature image (7/23/2014). Image shows four principal centers of ammonia emission. (b) LWIR hyperspectral map of the eight most common minerals for the F1 and F2 fumarole fields superimposed on gray-scale thermal radiance image (7/23/2014).

at F2NC where ground truth specimens returned to the laboratory confirmed the remote sensing identifications.

Typically more than one mineral was identified in the ground truth samples, which may have included subsurface minerals being incorporated into the material being analyzed. Mineralogical inhomogeneities also certainly existed on the scale of the SEBASS/Mako GSD (0.5–1 m). In general the spectrally dominant mineral identified by Mako represented the major mineral identified by XRD, with the exception of blödite. The first two ground truth surveys failed to identify any blödite based on random sampling, including when multiple spectra were recorded with the Exoscan in the field. The verification of blödite was somewhat problematical because the blödite formed scattered subtle mm-sized growths that were not obvious when sampling the surface that was predominantly quartz sand and halite. It covered only a small fraction of the area of the pixels mapped as blödite but was more obvious beneath the surface in cross sections. In contrast, the other sulfate minerals formed substantial easily recognizable accumulations. It was not until the inconspicuous blödite could be recognized in the field that successful ground truth samples were collected. In areas mapped as blödite, quartz sand and halite represented the mean scene vector in the remote sensing data which was subtracted before mineral identification. This is the likely reason why blödite was identified as the spectrally dominant mineral present in these areas even though it represented a very small pixel fill fraction.

The results of ground truth surveys by Vaughan et al. (2005) for SEBASS data from the Steamboat Springs geothermal field were similar to ours from the Salton Sea fumaroles. They found that XRD generally identified the major mineral mapped remotely as the dominant component in a mixture of minerals. Failures of the ground truth could be attributed to spectra of minerals identified by XRD not being in the remote spectral library, inhomogeneities at the sampling site and the drastically different length scales between the collected samples and remote ground sampling distance.

The ground truth survey verification of the minerals (blödite, thenardite, mascagnite) identified along the brush line was only partially successful, in part because the area was saturated with briny water and very soft and muddy. Collected samples that were returned to the lab tended to crystallize halite and were not representative of the material present on the surface at ~41 °C when the Mako flight was conducted. SEM/EDS of cross sections was helpful in identifying blödite and thenardite that was below the surface of collected samples. It was not practical to perform Exoscan traverses to prescreen samples in real time for return to the lab because of the distance between the collection area and a base lab on solid ground. Mascagnite was not expected along the brush line since there were no obvious white deposits like at F1 and to a lesser degree F2. It is noted that there are small areas of gaseous emissions along the brush line as evidenced by slow bubbling.
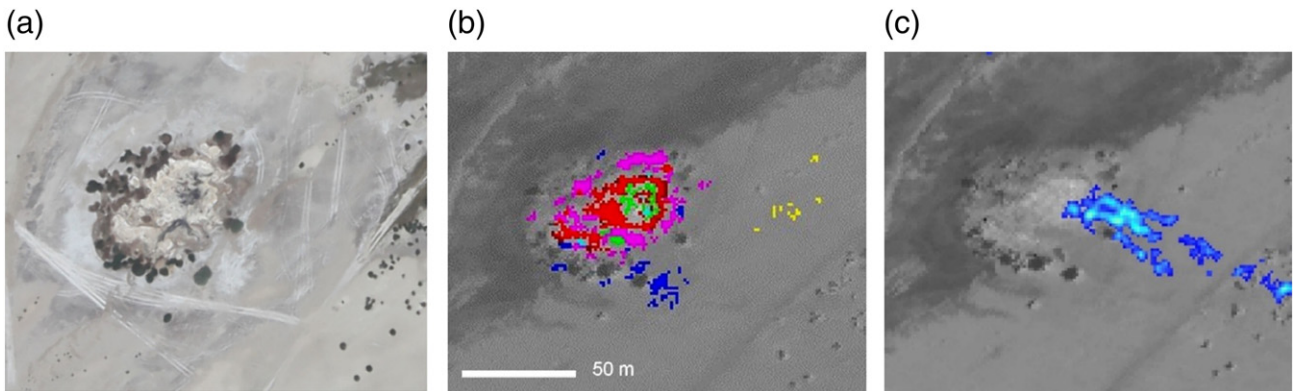

Fig. 15. (a) Context camera view of fumarole field F1 (4/22/2015). (b) Detail of mineral map of F1 superimposed on gray scale surface brightness temperature image (7/23/2014). Red = mascagnite, green = gypsum, magenta = nitratine, blue = blödite and yellow = thenardite. (c) Map of ammonia plume. Plume originates at left-most spot centered in the gypsum zone (green) and is blown to the southeast.
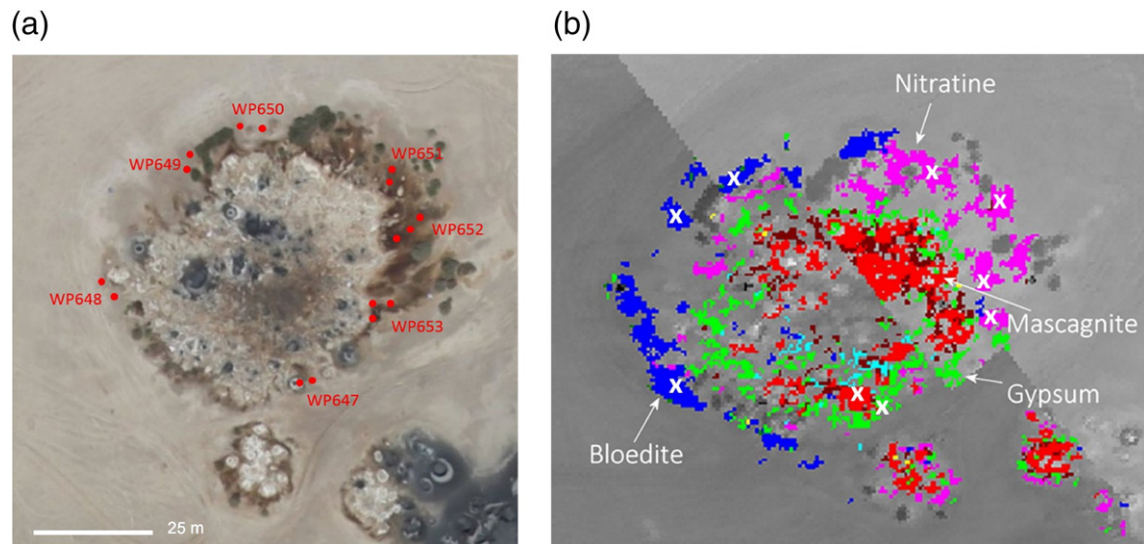
Fig. 16. (a) Context camera view of F2NC fumarole field (9/24/2015). (b) Detailed LWIR hyperspectral mineral map for the F2NC fumarole field superimposed on gray-scale thermal radiance image (9/24/2015). Red = mascagnite, green = gypsum, magenta = nitratine, blue = blödite, brown = boussingaultite and cyan = epsomite. X's mark locations where ground truth/laboratory analyses verified remote sensing identifications. Note distortion of the mineral map as a result of georeferencing errors between the two stitched flight lines.

Based on these confirmations we are confident in interpreting the remote sensing results over the evolution of the fumarole fields. The successful ground truth survey in September 2015 was in part a result of lessons learned from previous less fruitful attempts. The first attempt in October 2013 was the least successful. It relied upon using GPS coordinates from completed georeferenced mineral maps coupled with GPS location of sampling locations in the field. Georeferencing errors in producing the maps (± 10 m), errors in GPS location in the field (± 2 m) and the fact that the ground truth survey was conducted one month after the remote collect all contributed to the poor verification results. The use of the aluminum foil panels in September 2015, which were visible in both the context camera and LWIR images, made locating specific areas for sampling more accurate than depending on georeferencing the mineral maps and relying on the ± 1–2 m resolution of handheld GPS. Having the TAR single component mineral images delivered the same day as the data collect also made locating particular mineral zones easier. When areas were inhomogeneous the use of the

Exoscan made it possible to do near real time preliminary mineral identifications in the field, thereby increasing the probability of collecting the correct material for lab identification by XRD. Prompt laboratory analyses also minimized the possibility that sample mineralogy could change over time. All of these factors are important for these evaporite minerals because of the inhomogeneity of the deposits (both on the surface and subsurface) and their ephemeral nature. The latter, on the scale of weeks to months, is dependent on rainfall, temperature, and agricultural runoff levels. On much shorter time scales one must be aware that the temperature of the actual ground surface (outer 10s of microns) during the remote sensing collect may have easily been >60 °C (maximum air temperatures were 42–47 °C). Ground surface temperatures as high as 71 °C have been recorded in several places in Death Valley, CA with the record being 88 °C (Robinson and Hunt, 1961). The sand/mud substrates, part of which are collected with samples returned to the lab, may have been saturated with brine. Once returned to the lab where the temperature was about 20 °C the brine has the opportunity to migrate to the surface through capillary action and dissolve existing minerals or precipitate new species. Most of the sulfate minerals are highly water soluble, with the solubility

Table 3
Ground truth mineral identifications for fumarole field F2NC from Fig. 16 (9/24/2015).

Way point	Sample	Mako ID	Exoscan ID	XRD ID
647	A	Mascagnite	Mascagnite	**MASCAGNITE**, lecontite
	B	Gypsum	Gypsum	**GYPSUM**, QUARTZ, mirabilite
648	A	Blödite	Blödite	QUARTZ, Halite, **blödite**
	B	Blödite	Blödite	QUARTZ, Glauberite, **blödite**
649	A	Blödite	Quartz, Halite	HALITE, Quartz
	B	Blödite	Blödite	QUARTZ, halite, **blödite**
650	A	Blödite	Quartz, Halite	QUARTZ, Halite
	B	Blödite	Blödite	HALITE, Quartz, **blödite**
651	A	Nitratine	Nitratine	QUARTZ, **NITRATINE**, Glauberite, Anhydrite
	B	Nitratine	Nitratine	**NITRATINE**, Quartz, Anhydrite
652	A	Nitratine	Nitratine	**NITRATINE**, Quartz, Anhydrite
	B	Nitratine	Nitratine?	ANHYDRITE, **NITRATINE**, QUARTZ, gypsum
	C	Nitratine	Nitratine	**NITRATINE**, Quartz, Anhydrite
653	A	Nitratine	Nitratine +?	QUARTZ, ANHYDRITE, Halite, nitratine?
	B	Nitratine	Blödite?	QUARTZ, HALITE, glauberite, bassanite
	C	Nitratine	Nitratine +?	**NITRATINE**, Anhydrite, quartz

XRD Abundance: MAJOR, Minor, trace.
Bold = XRD verification of Mako mineral map.

Table 4
Ground truth mineral identifications for northwest fumarole field F2BC (9/24/2015).

Way point	Sample	Mako ID	Exoscan ID	XRD
654	A	Blödite	?	QUARTZ, Halite, **blödite**
	B	Blödite	?	QUARTZ, Halite, **blödite**
	C	Blödite	Quartz	QUARTZ, Halite, **Blödite**
655	A	Boussingaultite		**BOUSSINGAULTITE**, Koktaite
	B	Boussingaultite		**BOUSSINGAULTITE**
	C	Nitratine	Quartz, Nitratine	QUARTZ, **NITRATINE**, Blödite
	D	Nitratine	Quartz	QUARTZ, Hexahydrite
656	A	Boussingaultite	NA	QUARTZ, Koktaite, **Boussingaultite**
	B	Boussingaultite	NA	**BOUSSINGAULTITE**
657	A	Boussingaultite	NA	MASCAGNITE, QUARTZ, sal ammoniac, koktaite
	B	Boussingaultite	Gypsum	GYPSUM
	C	Boussingaultite	NA	QUARTZ, **Boussingaultite**, lecontite

XRD abundance: MAJOR, Minor, trace.
Bold = XRD verification of Mako mineral map.
NA = not analyzed.

Table 5
Solubilities[a] in pure water at 25 °C of the most common fumarole field minerals.

Mineral	Solubility (g/kg)
Gypsum	2.08
Anhydrite	3.11
Glauberite	118.2
Boussingaultite[b]	179
Mirabilite	273.5
Halite[b]	357
Epsomite	358.3
Thenardite	519.9
Blödite	522.5
Mascagnite[b]	706
Nitratine[b]	921

[a] Spencer (2000).
[b] Handbook of Chemistry and Physics, CRC Press.

dependent on temperature (Table 5) so the possibility exists for dissolution or precipitation after samples were collected. There were early examples where field Exoscan spectra of samples could not be duplicated several weeks after the samples had been returned to the lab.

4.2.3. Evolution of fumarole mineral fields

As stated earlier there is a concentric distribution of minerals centered on areas with the boiling pools and sulfur forming vents (Figs. 11, 15b, 16b). Outwardly from the pools/vents they have been divided into the following three zones where the dominant minerals are given in parentheses: fumarole (mascagnite, gypsum, boussingaultite), transition (nitratine) and evaporite (blödite, thenardite).

Fig. 17 presents the mineral maps for F2NC for the period of 2009 through 2017. Blödite, thenardite and gypsum are the first minerals to form (2009) and significant amounts of ammonium containing minerals (mascagnite, boussingaultite) do not appear until 2013 even though ammonia emissions from the location were noted as early as
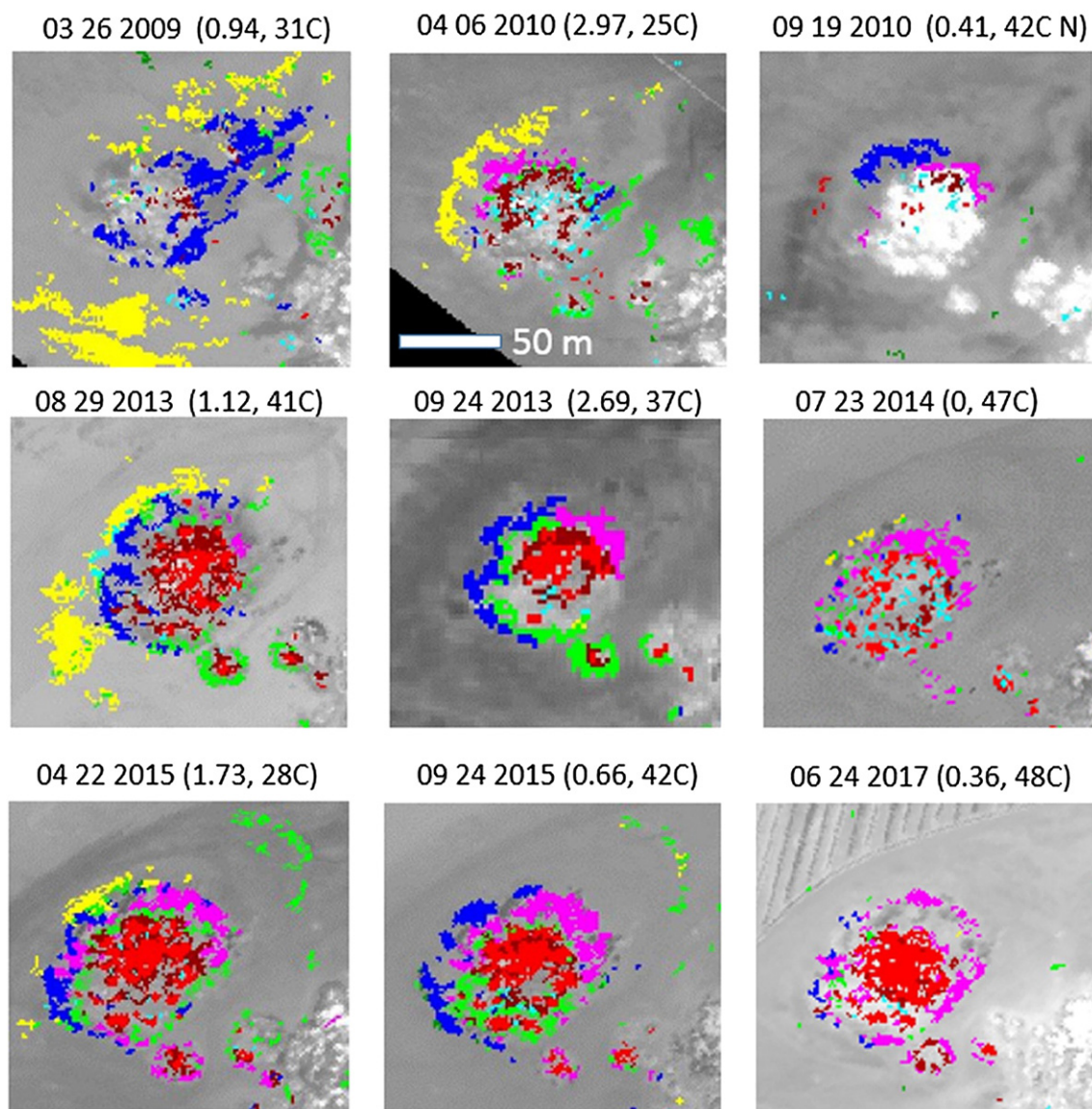
Fig. 17. Time series of mineral maps for the F2NC fumarole field superimposed on gray-scale thermal radiance images. Dates of data collects are given along with total rainfall (in cm) in the prior three months and the daily high temperature (°C), respectively, in parentheses. Note that 9/19/2010 was a night time collect (N). Red = mascagnite, green = gypsum, magenta = nitratine, blue = blödite, brown = boussingaultite, cyan = epsomite and yellow = thenardite.
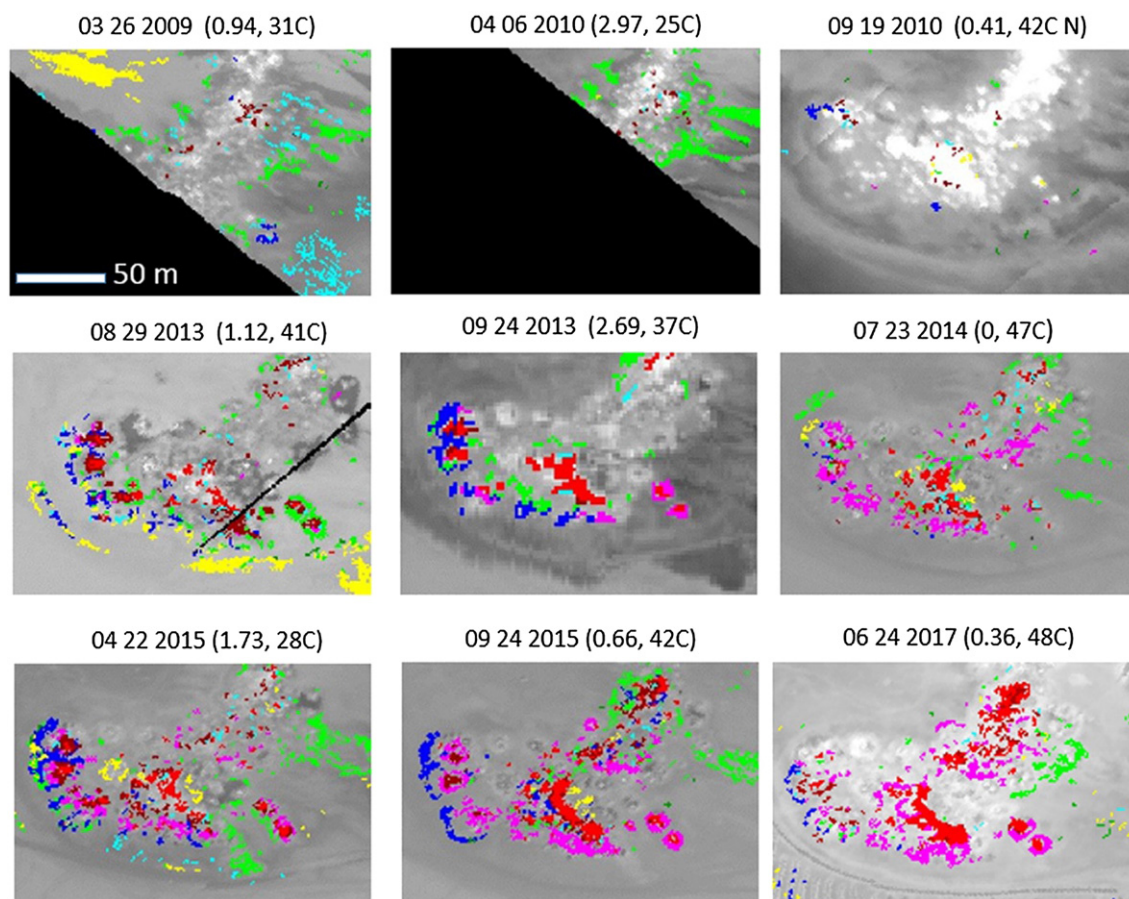
Fig. 18. Time series of mineral maps for the F2BC fumarole field superimposed on gray-scale thermal radiance images. Dates of data collects are given along with total rainfall (in cm) in the prior three months and the daily high temperature (°C), respectively, in parentheses. Note that 9/19/2010 was a night time collect (N). Red = mascagnite, green = gypsum, magenta = nitratine, blue = blödite, brown = boussingaultite, cyan = epsomite and yellow = thenardite.

2009 (Tratt et al., 2011). This is consistent with ground observations. The previously mentioned concentric ring structure is even present at that time and in general there are only subtle changes in its structure over time. The most noticeable difference was on 23 July 2014 when the amounts of mascagnite, gypsum and particularly blödite were greatly diminished. This corresponded to a time with no appreciable rainfall (0.05 cm) in the preceding seven months and relatively high temperatures (>40 °C) at the time of the collect, which implied that the fumarole field was relatively dry. Epsomite also appeared to be more common in that time frame. The observations on 6/24/17 are somewhat similar to those of 7/23/17 in that the occurrence of gypsum and blödite are very low but mascagnite is still common. Both dates had the highest temperatures of all the collects and followed periods of relatively low rainfall.

A time series of mineral maps for the F2BC field is presented in Fig. 18. The same general trends from F2NC are repeated here with gypsum appearing as early as 2009. Similar concentric rings of minerals are also seen at the southwestern end of F2 but they are not as completely developed as in F2NC (Figs. 16b, 17). Gypsum, epsomite and thenardite are the first minerals to appear in significant quantities. Boussingaultite is the first ammonium mineral to form (along with nitratine) and is found with the other magnesium-containing sulfate — epsomite. Mascagnite does not appear in quantity until 2013. As with F2NC there is less sulfate mineralogy present during July 2014 and June 2017 with blödite being nearly absent. A distinctive feature of the rings is that they are commonly incomplete. At both the F2NC and F2BC fields blödite is typically only found on the west side, while at the F2NC field nitratine is more concentrated on the NE side.

The F1 field also shows mineral zonation (Fig. 19) but it is slightly different from F2. The first presence of ammonium minerals (mascagnite) was mapped in September 2010 which is consistent with the first field observations in 2011 but is earlier than that observed at F2. Nitratine did not become a prominent mineral until 2013 and there is a considerable difference between August and September 2013 with the latter having considerably more nitratine and being just after a much wetter period. In June 2017 nitratine is nearly absent as a result of the former transition zone being submerged under several cm's of water. Unlike at F2, gypsum periodically (7/2014, 9/2015) forms the core of the concentric rings and appears to be more prevalent during drier periods (7/2014, 9/2015). While being common in 2010, blödite was subsequently more scattered and intermittent and in 2017 its occurrence shifted from the east side to the west side as a result of flooding of the area surrounding F1.

Fig. 20 shows the mineral maps for the F2 eastern brush/shore line area. This area does not show obvious fumarole activity or significant non-halite salt accumulations and the shoreline has changed significantly from 2013 to 2015. While the overall Salton Sea level has dropped during this period, the area of the marsh has increased and migrated westward since late 2014. The Sonny Bono National Wildlife Refuge is located several kilometers south of the fumaroles and the area in general has a high population of waterfowl. As the Salton Sea level has dropped there has been a large decrease in waterfowl habitat and sportsmen (duck hunters) have attempted to reverse this trend by damming agricultural runoff, thereby increasing the marsh area to the east of the fumaroles. Subsequent to 2015 the development of dust mitigation trenching has greatly expanded the marsh westward.
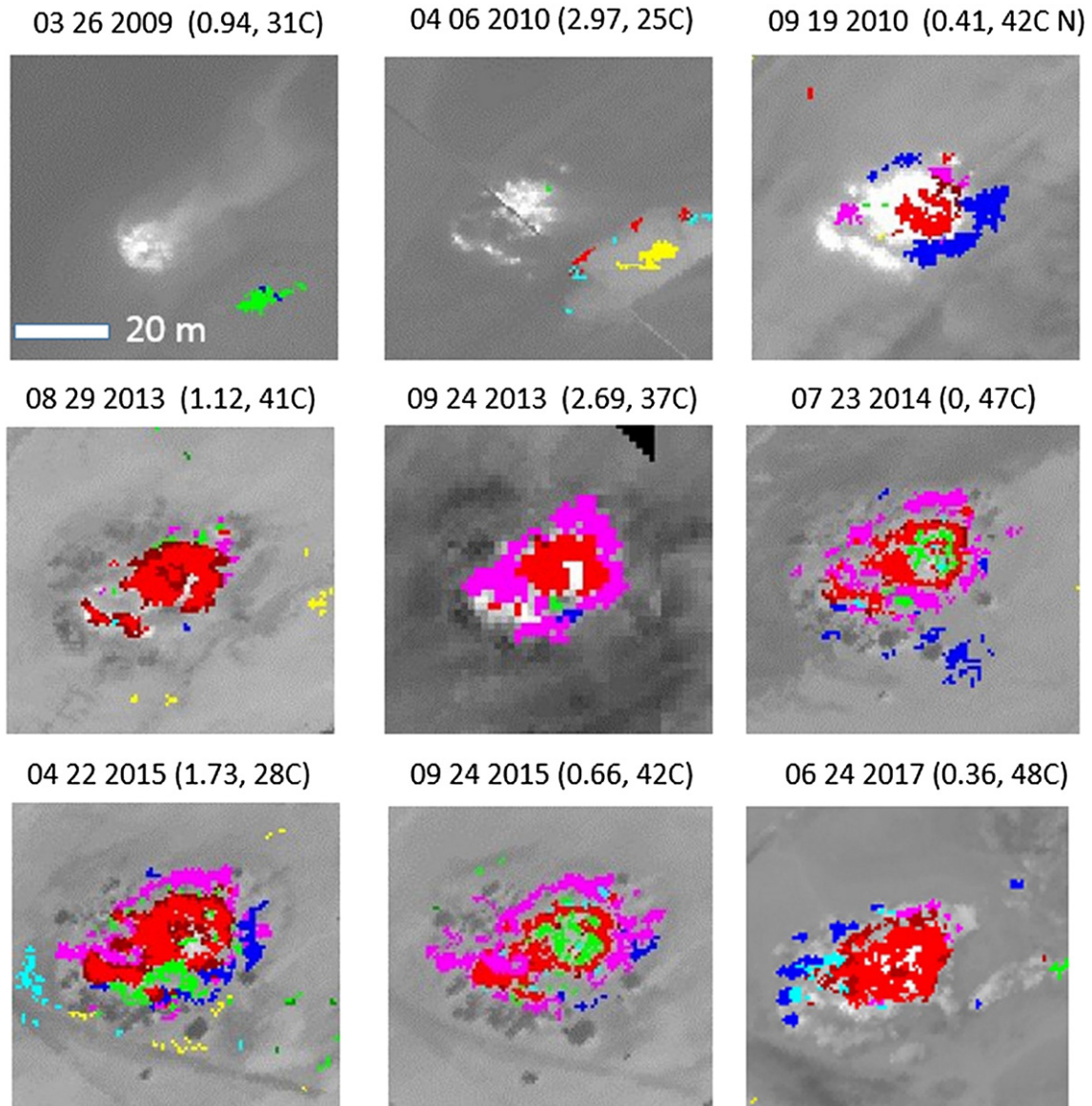
Fig. 19. Time series of mineral maps for the F1 fumarole field superimposed on gray-scale thermal radiance image. Dates of data collects are given along with total rainfall (in cm) in the prior three months and the daily high temperature (°C), respectively, in parentheses. Note that 9/19/2010 was a night time collect (N). Red = mascagnite, green = gypsum, magenta = nitratine, blue = blödite, brown = boussingaultite, cyan = epsomite and yellow = thenardite.

Blödite, thenardite and gypsum have commonly been mapped along the brush/shore line. Mascagnite has also been locally mapped but has not been ground truth verified and in general, ground truth surveys of this area have been less successful because the area is very muddy with very shallow standing water (see Section 4.2.2). In very shallow water small bubbles have locally been seen indicating there are limited gas emanations in the area. On November 23, 2013 extensive crusts of thenardite, often with or after mirabilite were observed on the west side of F2 complex and the F2 SE brush line mud flats. Along the latter they usually encrusted the stems of dead vegetation. This time period was shortly after a very heavy rainfall (2.7 cm). This indicates that it is not unreasonable to expect these minerals along the brush line.

Fig. 21 shows the context camera image and mineral map for the wind borne dust mitigation trenches and the brush/shore line area south of F2 on 6/24/2017. The easternmost trenches have been partially filled with water as shown by the dark coloration in both the visible and LWIR images. Along the southeast shoreline a variety of sulfates have been identified, including anhydrite, gypsum, thenardite, blödite and mascagnite similar to those seen in Fig. 20. Surprisingly gypsum and,

to a lesser degree blödite, were identified along some of the trenches. It is not known whether these were present subsurface and were exposed in the trenching process or if they formed by precipitation from newly introduced fluids brought to the surface by capillary action.

4.2.4. Comparison with other remote sensing studies

Reath and Ramsey (2013) published a partial mineral map for the F2 fumarole field from the same SEBASS data presented in this paper, referring to the area as the "Sand Bar" field. A direct comparison with our data is shown in Fig. 22. There is satisfactory agreement in the areas identified as gypsum between our map and Reath and Ramsey (2013), but there are also two significant respects in which the two analyses diverge and that merit further discussion. Firstly, we did not identify significant amounts of anhydrite in the F2 region of interest but some of the areas identified as anhydrite by Reath and Ramsey (2013) were mapped as blödite or thenardite. It is noted that we did identify small regions of anhydrite on the surface along the brush line east of F2. This was not verified by ground truth but anhydrite was identified by XRD in subsurface material from the transition zone. Secondly, one of Reath and
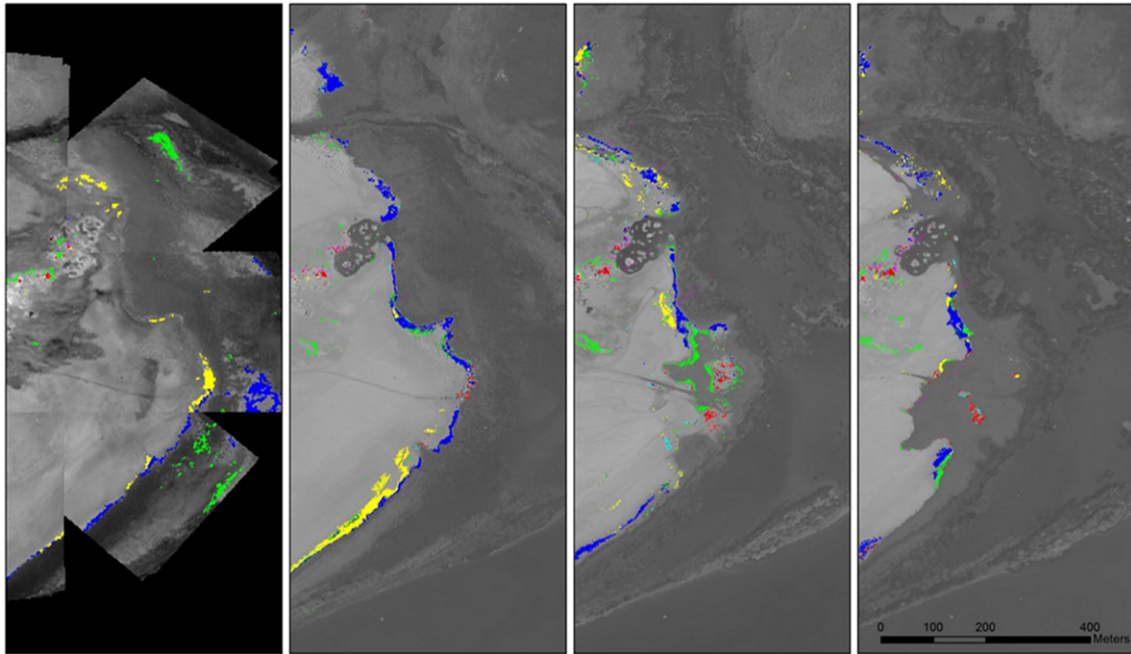
Fig. 20. Detailed LWIR hyperspectral mineral maps for the brush line area from 9/24/2013 to 9/25/2015. Dates of data collects are given along with total rainfall (in cm) in the prior three months and the daily high temperature (°C), respectively, in parentheses. Dark area to the east is water. Red = mascagnite, green = gypsum, magenta = nitratine, blue = blödite, cyan = epsomite and yellow = thenardite.

Ramsey's (2013) major conclusions was that an unidentified Mg-sulfate was prevalent at the Davis-Schrimpf and F2 fumarole fields (red in Fig. 22, center). Their tentative identification of a probable Mg-sulfate was based on the presence of an 8.2 μm-doublet emissivity minimum in the SEBASS data, however they were unable to identify any Mg-containing sulfates during laboratory analyses that were carried out on material collected from those areas.

To explain these discrepancies it is instructive to review how the data were processed. In contrast to how mineral maps were generated for this paper (Section 2.1), Reath and Ramsey (2013) processed the SEBASS data

in the following manner: after atmospheric compensation a decorrelation stretch (DCS) was used to display variations in emissivity (composition). Spectral variability within the SEBASS scene was then compared with sulfate spectra in the ASU and ASTER spectral libraries. Using the pixel purity index function in ENVI, a spectrum representing the unidentified hydrated Mg-sulfate mineral was identified in the SEBASS scene and incorporated into the end member suite of candidate minerals based on those reported from the Salton Sea area and observed in the SEBASS data. This spectral end member suite was then applied to the SEBASS emissivity data using the linear deconvolution modeling approach of Ramsey and
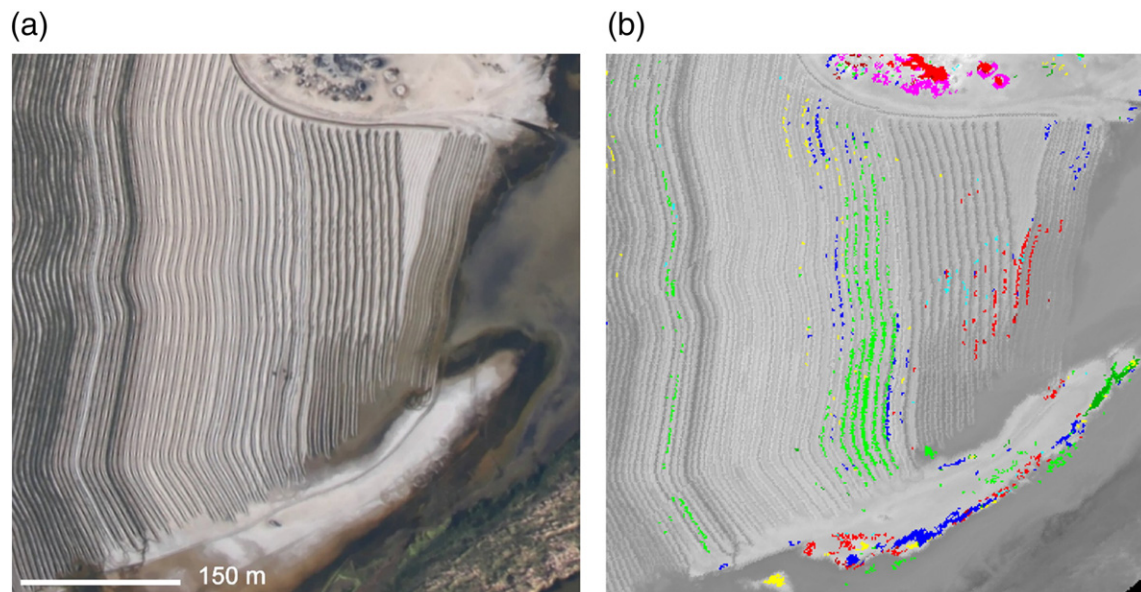

Fig. 21. Brush line area and dust mitigation trenches south of F2BC from 6/24/2017. (a) Context camera image. (b) Detailed LWIR hyperspectral mineral maps for the trenches. Red = mascagnite, lime green = gypsum, magenta = nitratine, blue = blödite, cyan = epsomite, dark green = anhydrite and yellow = thenardite.
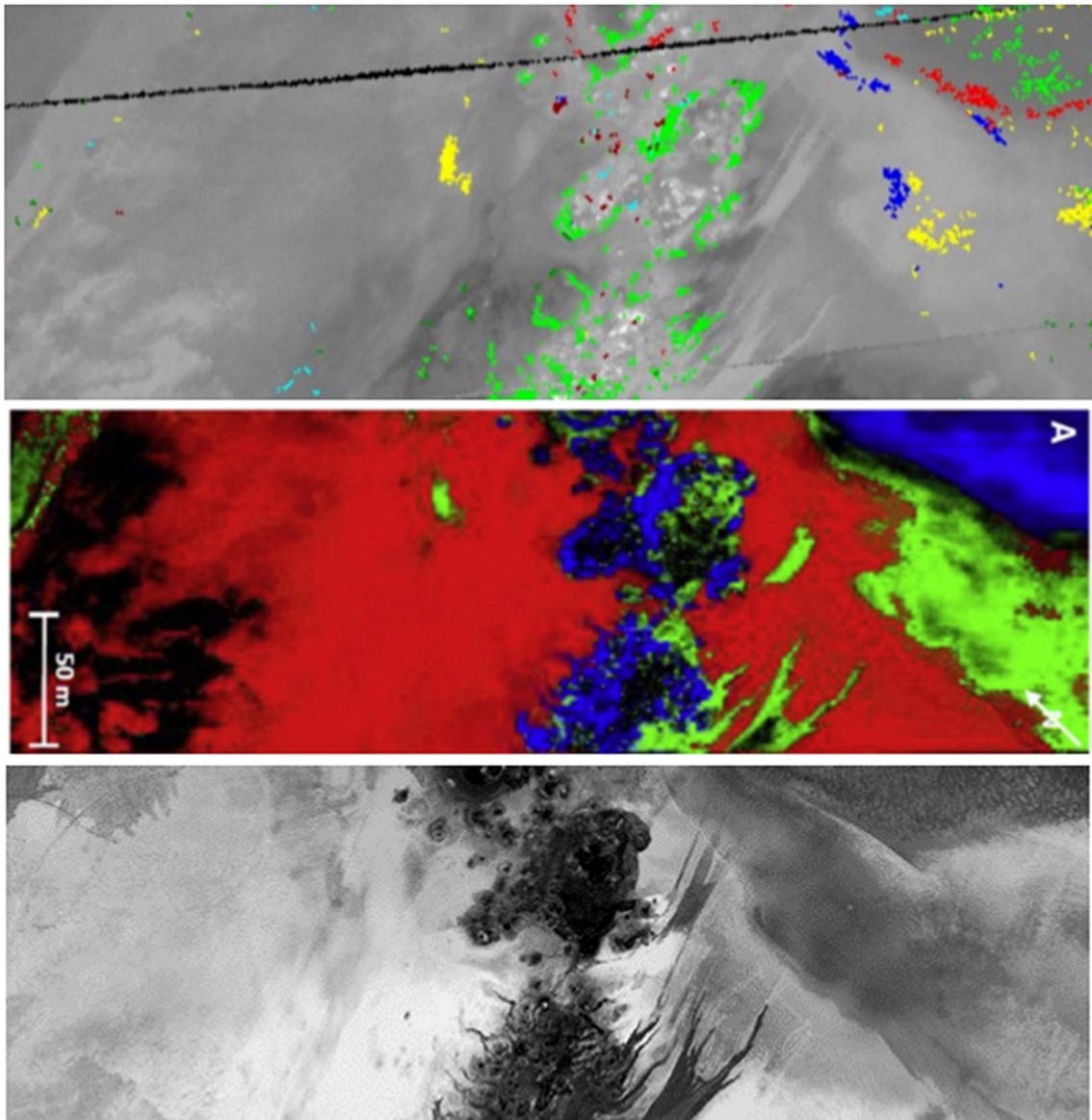
Fig. 22. Northeast fumarole field F2BC 4/6/2010 SEBASS data collect. (top) Aerospace SEBASS mineral map superimposed on gray-scale thermal radiance image. Red = mascagnite, lime green = gypsum, magenta = nitratine, blue = blödite, brown = boussingaultite, cyan = epsomite, dark green = anhydrite and yellow = thenardite. (center) Mineral map from Reath and Ramsey (2013) of the same SEBASS scene. Red = unknown Mg sulfate, green = anhydrite and blue = gypsum. (bottom) Aerospace panchromatic context camera image.

Christensen (1998). Spectral variability (e.g. DCS) within the SEBASS/Mako data were not evaluated before creating our maps so that regions with spectra not accounted for in the Aerospace solids library could not be identified. Since the solids library only contains spectra of known minerals, regions such as the putative Mg-sulfate would not be mapped.

Fig. 23 compares the spectra derived from the SEBASS data for areas identified as gypsum, anhydrite and the unknown Mg-sulfate by Reath and Ramsey (2013) in Fig. 22. It can be seen that gypsum areas have a very strong band with significant spectral contrast and it was mapped by both us and Reath and Ramsey (2013). In contrast, the anhydrite signature is very weak and shows very little spectral contrast with two broad poorly defined features. It is conjectured that in producing their mineral map Reath and Ramsey (2013) deconvoluted a fine grained anhydrite spectrum from this data since it also has very low spectral contrast. They indicated that anhydrite is expected in the Salton Sea area but provided no ground truth verification, whereas our mineral identification algorithm registered an insufficient signal to noise ratio to retrieve a positive identification with acceptable confidence.

Turning now to the 8.2 μm feature that Reath and Ramsey (2013) hypothesized as a probable unidentified Mg-sulfate, we advance an alternative explanation. This area is part of what we have referred to as the evaporite zone which, with the exception of localized areas of blödite and thenardite, typically has a thin halite crust overlying quartz sand. Representative examples of Exoscan spectra from this zone (albeit from a slightly different location and at a much later date) are presented in Fig. 24a. In some of the spectra a reflectance maximum near 8.16 μm is present. This is very close to the feature reported by Reath and Ramsey (2013) but is not a doublet. Our interpretation hinges on the observation that halite can modify the characteristic quartz spectrum in such a way that a shoulder results at 8.16 μm. We did not perform a ground collect in the 2010 time frame but a color aerial image (Fig. 25) shows the area surrounding F2 to be bright white similar to a halite covered salt pan. This further supports the idea that halite is present in the area at that time.

Fine-grained wind-blown quartz, or another silicate such as a clay entrapped in the halite, may be responsible for the observed spectra.
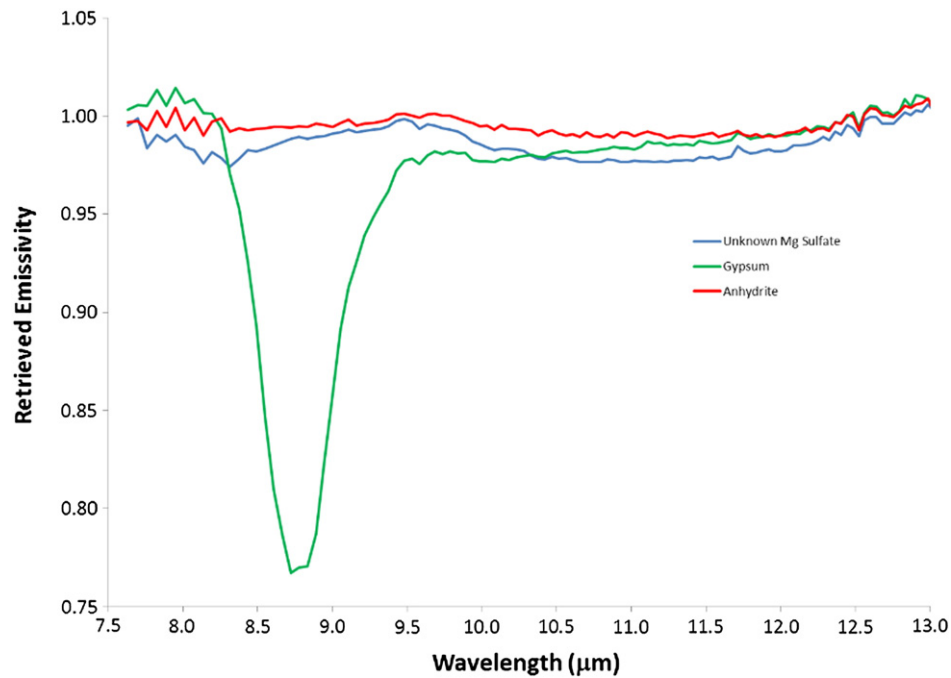
Fig. 23. Spectra derived from SEBASS data for areas identified as gypsum, anhydrite and unknown Mg-sulfate by Reath and Ramsey (2013) in Fig. 22b. Spectra are an average of 10–20 pixels.

Halite is spectrally featureless in the LWIR (Eastes, 1989) but its presence does appear to influence the spectrum of quartz sand, which is ubiquitous in the areas surrounding the fumaroles. The amount of halite/fine grained quartz modifies the quartz spectrum to differing degrees. In particular, the lobe of the quartz band at 9.65 μm decreases with increasing amounts of halite/fine grained quartz while the lobe at 8.4 μm remains relatively unchanged. Fine grained powders, dilutely dispersed in an IR transparent medium (KBr, NaCl), produce transmission-like features in diffuse reflectance of spectra (Fuller and Griffiths, 1978; Sobkowiak and Painter, 1995).

This can be better understood by considering the diffuse reflectance infrared Fourier transform (DRIFT) spectroscopy technique (Fuller and Griffiths, 1978). In this method a fine-grained powder is dispersed and diluted in an infrared transparent matrix (typically KBr). The diffuse

reflectance spectrum of this mixture produces a transmission-like spectrum as a result of the IR beam passing through the fine powder and diffusely reflecting off the KBr matrix particles. This phenomenon has been demonstrated by Eastes (1989) for halite mixtures with calcite, gypsum, quartz and montmorillonite. In contrast Berger et al. (2015) investigated the effect of pure halite coatings on materials and noted that the main result was to reduce spectral contrast and overall reflectance. In the case of the fumarole fields, very fine grained quartz may become trapped in NaCl, which then overlays coarse grained sand.

Laboratory spectra were recorded to test the fine grained quartz/halite hypothesis. Approximately 5 wt.% of <75 μm quartz powder was dispersed in fine-grained KBr (Sigma-Aldrich, FTIR grade). The diffuse reflectance spectrum of this mixture is shown in Fig. 24b (green) and is similar to that reported by Eastes (1989). Rather than a reflectance
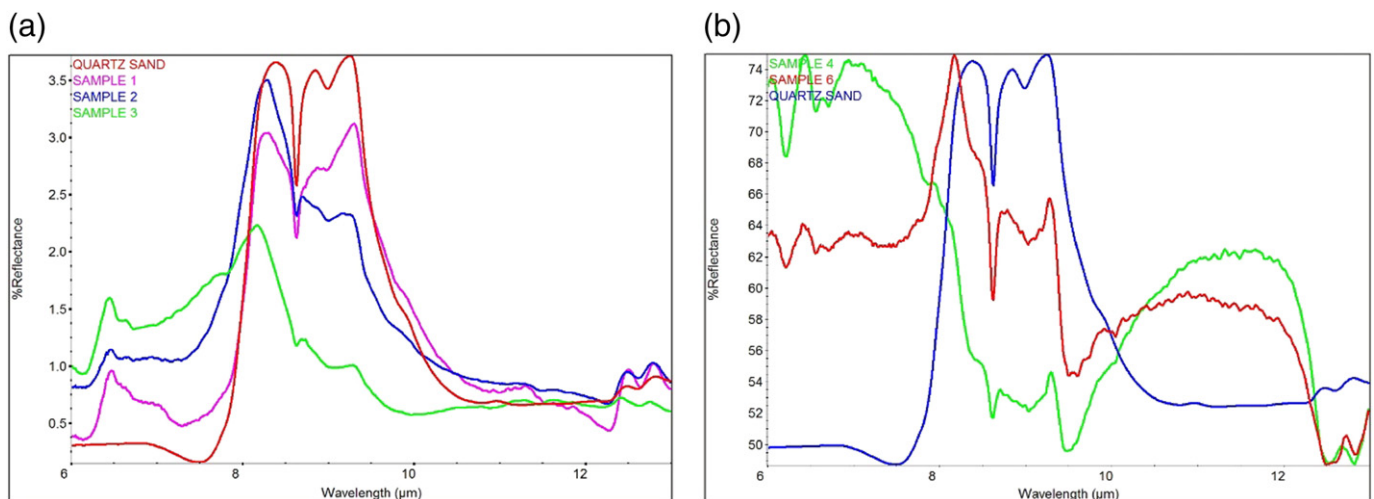

Fig. 24. (a) Exoscan reflectance spectra from the distal halite-containing portion of the evaporite zone from F2BC. Samples 1–3 contain varying amounts of what are assumed to be fine-grained quartz entrapped in halite on quartz sand. Scales have been adjusted for better comparison. The intensity of the 9.65 μm band decreases as the amount of entrapped fine grained quartz in halite, which has an absorption signature, increases. (b) Biconical reflectance spectra of coarse quartz sand (blue), dilute fine quartz (<75 μm) dispersed in KBr (green) and dilute fine quartz (<75 μm) dispersed in KBr dispersed on sand (red). Spectra scaled for better comparison.
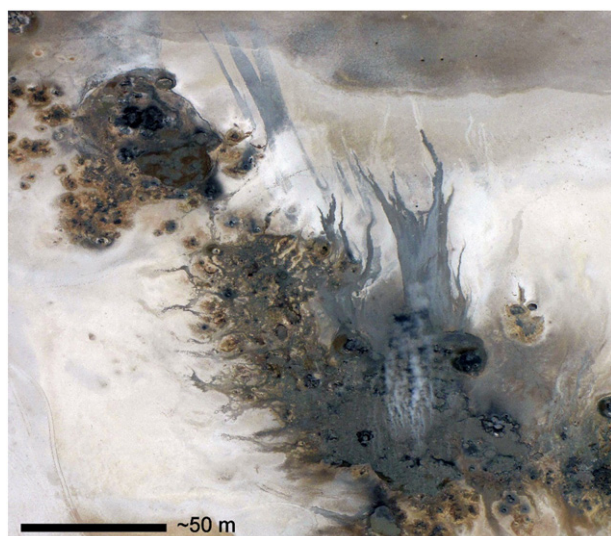
Fig. 25. Color aerial image of F2 fumarole field in Fig. 3 (Lynch et al., 2013). Note outflow of thin gray mud from bubbling pools and fumarole vents onto the white salt pan. Compare with Fig. 22 (bottom).

maximum, a reflectance minimum is produced at the location of the quartz reststrahlen band but it is shifted to slightly longer wavelength. When this feature is combined with the diffuse reflectance spectrum of coarse quartz sand the net effect is to drastically reduce the depth of the 9.65 μm band, with less of an influence on the 8.4 μm lobe, thus producing spectra similar to those shown in Fig. 24a. This was accomplished experimentally by placing a thin layer (<0.5 mm) of the <75 μm quartz and KBr mixture over the coarse quartz sand (red in Fig. 24b). By changing the thickness of the mixture the degree of the effect can be varied. Fig. 26 compares the results from the laboratory mixture (red) with an Exoscan spectrum (blue) in the field and a converted SEBASS spectrum from the unknown Mg-sulfate area. They are very similar considering that the exact composition and particle size of silicates mixed with halite in the field is not known. We believe that this phenomenon is responsible for the 8.2 μm feature Reath and Ramsey (2013) mapped and tentatively identified as a Mg-sulfate and furthermore is consistent with their not
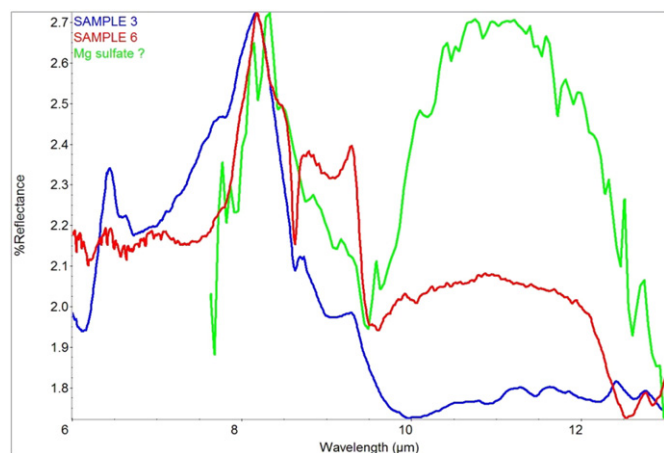

Fig. 26. Comparison of SEBASS spectrum of putative unknown Mg-sulfate with laboratory and field spectra. Spectra scaled for better comparison. SEBASS spectrum (green) was converted to reflectance using Kirchhoff's Law ($R = 1 - \varepsilon$). Sample 3 (blue) is an Exoscan reflectance spectrum from the distal halite-containing portion of the evaporite zone and contain varying amounts of what are assumed to be fine-grained quartz entrapped in halite on quartz sand. Sample 6 (red) is a laboratory biconical reflectance spectrum of dilute fine quartz (<75 μm) dispersed in KBr and dispersed on quartz sand.

being able to identify a Mg-sulfate in laboratory analyses of the ground truth samples. They noted only that XRD failed to identify any minerals consistent with the LWIR signature. The 8.2 μm feature was not a doublet and was slightly shifted in their emissivity measurements, which they attributed to the elevated temperatures associated with the analysis, possibly dehydrating the mineral of interest.

Eastes (1989) concluded that the spectral properties of minerals mixed with NaCl can be significantly different from the pure materials and the spectral behavior cannot be predicted with confidence from the transmission or reflectance spectra of the separate constituents. Furthermore they indicate that remote sensing of highly saline environments may need to consider the potential spectral effects of NaCl since it is common to those regions.

4.3. Field infrared spectroscopy

A total of 11 diffuse reflectance Exoscan traverses were performed. In many instances it was difficult to obtain spectra because of the very low signal resulting from the very irregular surfaces. Fig. 27 shows the location of an Exoscan traverse at the F1 field with the corresponding spectra in Fig. 28. This duplicates the zonation observed on a much larger scale in the remote sensing data. Gypsum was found closest to the sulfur producing vent followed by zones of boussingaultite, nitratine and blödite followed by quartz/halite. In other traverses the same general zonation was observed with the exception that blödite was often not observed.

5. Detailed mineral descriptions

The following mineral descriptions are arranged by zones approximately in the order they appear with distance from bubbling pools and sulfur producing vents.

5.1. Fumarole zone

The fumarole zone is located closest to ammonia emitting vents, boiling pools and gryphons. It is characterized by conspicuous accumulations of several different white ammonium sulfates, which are difficult to distinguish in the field, and gypsum.

5.1.1. Sulfur S

Dry hissing thermal vents up to 5 cm in diameter commonly have intergrowths of yellow bladed sulfur crystals associated with them (Fig. 9a) that appear to have formed by sublimation. The temperature measured in some of these vents was 100 °C. Dendritic growths of sulfur crystals have also been seen growing on dead vegetation (Fig. 29a). These vents are at ground level at F1 but at F2 they may also be near the summits, or on the flanks, of gryphons. Vents at F2 showing sulfur crystal growths became more common in 2014. The individual crystals range up to 3 mm in length and have a skeletal appearance (Fig. 29b). Beneath the surface, close to the vents, cavities (to 8 cm) in wet black mud often have a thin lining of sulfur crystals. Crude bladed gypsum crystals (to 0.5 mm) are often associated with, or in close proximity to, the sulfur crystals. Sulfur crystals associated with these fumarole vents have been documented as early as the late 1800s (Hanks, 1882).

5.1.2. Gypsum $CaSO_4 \cdot 2H_2O$

Gypsum appears to form in two different environments, one fumarole related and the other evaporite. Mats of white to cream-colored crude bladed gypsum crystals (to 1 mm) are often associated with sulfur producing vents and mascagnite (Fig. 30). Gypsum may also occur as fibrous aggregates and as clear thin fibers found underneath other sulfate crusts. Other associated species include boussingaultite, tschermigite and koktaite. Some gypsum-containing areas several meters from vents at F2 have been identified by remote sensing along with areas along the eastern brush/shore line.

Fig. 27. Northeast corner of fumarole field F1 with Exoscan traverse EX2 (1/2014) marked with arrows (0 m and 10 m relate to location distances of spectra in Fig. 28). White efflorescence at 0 m contains gypsum and boussingaultite and dark brown patch just left of center contains sodium nitrate (nitratine). White salt pan in the distance is primarily a surface coating of halite.

5.1.3. Mascagnite $(NH_4)_2SO_4$

White, cream or light gray botryoidal crusts of mascagnite covering areas of several square meters are relatively common and are often found close to sulfur producing vents and boiling pools at both F1 and F2 and may also be found growing on dead vegetation (Fig. 9a). The deposits can be up to several cm thick (Fig. 31a) and can vary from columnar growths with mushroom-like tops to unconsolidated material with the consistency of fresh snow. The mascagnite is typically very fine grained but bladed crystals to 0.2 mm have been observed (Fig. 31b). Mascagnite may also be associated with lecontite, boussingaultite, koktaite or sal ammoniac. Subsurface, the mascagnite often has a fibrous-columnar structure with fibers to several cm (Fig. 32a).

A specimen of columnar/fibrous mascagnite (including the substrate) approximately 2 m from a sulfur producing vent at F1 was sampled and cross sectioned. The results are presented in Fig. 32. The subsurface consists primarily of sand grains (quartz with minor plagioclase and potassium feldspar) and elemental sulfur (to 0.20 mm) cemented with massive mascagnite. The base of the columnar mascagnite includes koktaite

blades (to 0.40 mm) while the upper 30 mm consists of fibrous mascagnite with minor boussingaultite.

Mascagnite from other localities has been formed from sublimation from volcanic fumaroles and coal fires (Dunning and Cooper, 1993; Parafiniuk and Kruszewski, 2010; Masalehdani et al., 2009). The thickness (to 6 cm) of fibrous deposits at the Salton Sea fumaroles suggests that precipitation from solutions drawn to the surface by capillary action (efflorescence) may also play a part, considering the high solubility of mascagnite (Table 5). The fact that the area experiences up to 5 cm of rain annually also supports the idea that there can also be dissolution and reprecipitation of mascagnite.

5.1.4. Boussingaultite $(NH_4)_2Mg(SO_4)_2 \cdot 6H_2O$

Boussingaultite is often a constituent of botryoidal crusts associated with sulfur producing vents. It commonly occurs with mascagnite, lecontite, tschermigite, koktaite and blödite. Crystals are typically only a few tenths of a mm long but larger corroded bladed crystals (to 4 mm) have been found in unconsolidated material below other crusts at F1 (Figs. 30b, 33a). In limited cross sections, boussingaultite crusts formed over loosely consolidated sand and gypsum (anhydrite/bassanite) (Fig. 33b). Boussingaultite can form from the evaporation of solutions of ammonium and magnesium sulfates (Faust and Bloss, 1963) and may be the result of dissolved mascagnite interacting with magnesium sulfate solutions derived from the evaporite zone. However, minor amounts of boussingaultite were observed in evaporation residues from clear pools.

5.1.5. Lecontite $(NH_4,K)Na(SO_4) \cdot 2H_2O$

Botryoidal mascagnite crusts from F1 and F2 occasionally contain minor amounts of lecontite. It also occurs with boussingaultite at F2. Euhedral lecontite crystals (to 0.1 mm) have only been recognized in a few specimens of more pure lecontite from F1 (Fig. 34a). Lecontite can form from evaporation of solutions of $(NH_4)_2SO_4$ and sodium sulfates (Corazza et al., 1967) which may have resulted from dissolved mascagnite mixing with sodium sulfates from the evaporite zone.

5.1.6. Koktaite $(NH_4)_2Ca(SO_4) \cdot 2H_2O$

Minor amounts of koktaite have been identified with boussingaultite and mascagnite by XRD in samples from F1 and F2. It occurs as bladed crystals to 200 µm (Figs. 32b, 34b). It has not been recognized in hand
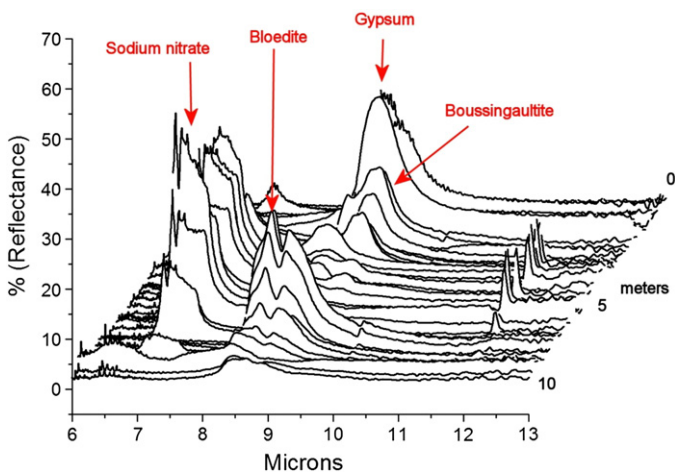

Fig. 28. Exoscan spectra from 10 m traverse EX2 (1/2014) in NE corner of F1 (refer to Fig. 27). A sulfur producing vent is located at 0 m. Sampling interval from 0 to 5 m was 15 cm; from 5 to 10 m interval was 30 cm.
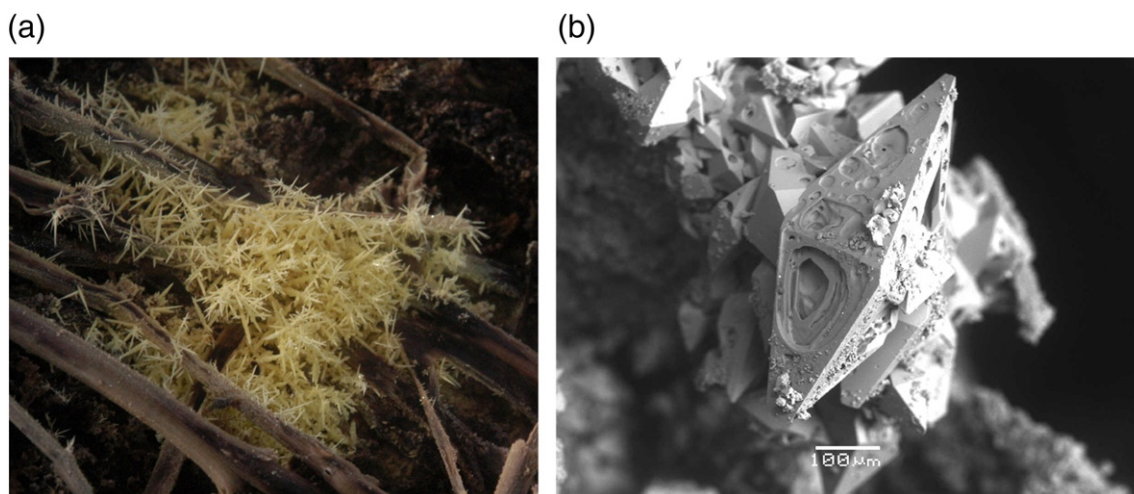
(a)

(b)

Fig. 29. (a) Dendritic sulfur growing on dead vegetation near an F1 thermal vent. Field of view is 9 cm. (b) SEM image of sulfur crystals.

specimens. It is assumed that it forms in a similar manner to boussingaultite and lecontite — by evaporation of solutions of ammonium and calcium sulfates.

5.1.7. Tschermigite $(NH_4)Al(SO_4)_2 \cdot 12H_2O$

XRD and SEM/EDS analyses have indicated that minor amounts of tschermigite occur with boussingaultite, lecontite and gypsum in samples from F1 and F2 (Fig. 35a, b). It has not been recognized in hand specimens.

5.1.8. Natrojarosite $NaFe_3^{3+}(SO_4)_2(OH)_6$

Small areas around vents at F1 and F2 have a yellow to light orange color. Natrojarosite occurs here as thin crusts of microscopic hexagonal plates (Fig. 36a).

5.1.9. Sal ammoniac NH_4Cl

Minor amounts of sal ammoniac have been identified with mascagnite by EDS from F2 (Fig. 36b). It also occurs in evaporation residues of water collected from hot milky pools at F2 (Table 2). It has not been recognized in hand specimens. Sal ammoniac specimens from the fumaroles were identified as early as 1850, by the subjective method of "the sharpness of their taste" (LeConte, 1855). Sal ammoniac is commonly produced by sublimation at fumaroles at many other worldwide occurrences (Parafiniuk and Kruszewski, 2010; Masalehdani et al., 2009).

5.1.10. Tamarugite $NaAl(SO_4)_2 \cdot 6H_2O$

Tamarugite was identified by XRD from one specimen with alum-(Na) in a sulfate patch at the SE end of F2 that also contained lecontite, mascagnite and boussingaultite. It has not been recognized in hand samples.

5.2. Transition zone

The transition zone is a typically brown nitrate-containing band on the surface that separates the ammonium sulfates of the fumarole zone from other sodium and magnesium sulfates of the evaporite zone.

5.2.1. Nitratine $NaNO_3$

In January 2014 an Exoscan FTIR survey of sulfate patches in the SE corner of F2 revealed the presence of nitratine. It was found in black and brown areas just outside of the ammonium sulfate growths around small bubbling pools and vents. These brown rings containing nitratine are very common and are associated with the more distal regions of small fumarole vents and the fumarole fields as a whole (Fig. 11). They constitute one of the more prominent remotely sensed mineral map units. Crystalline deposits, however, were inconspicuous in these
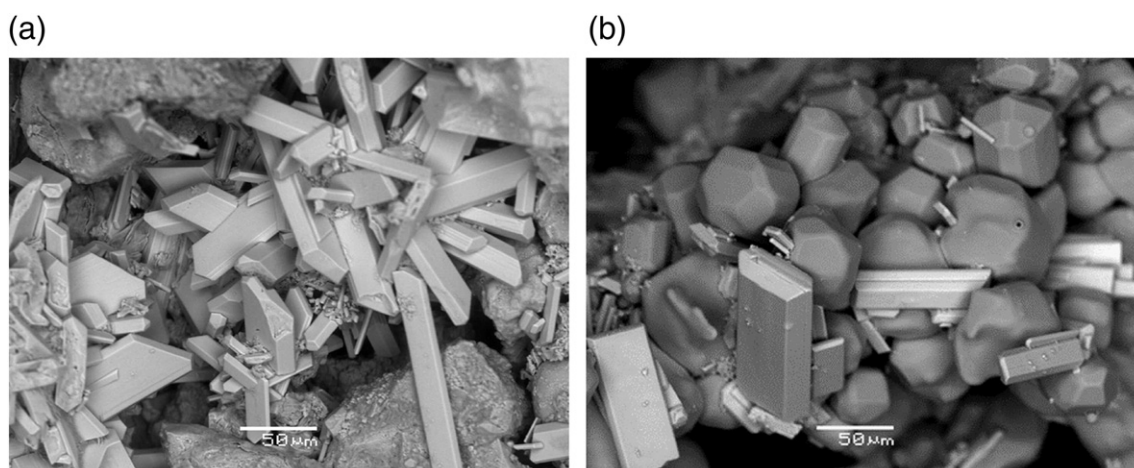
(a)

(b)

Fig. 30. (a) SEM image of bladed gypsum crystals from F2. (b) SEM image of boussingaultite and bladed gypsum crystals from F2.
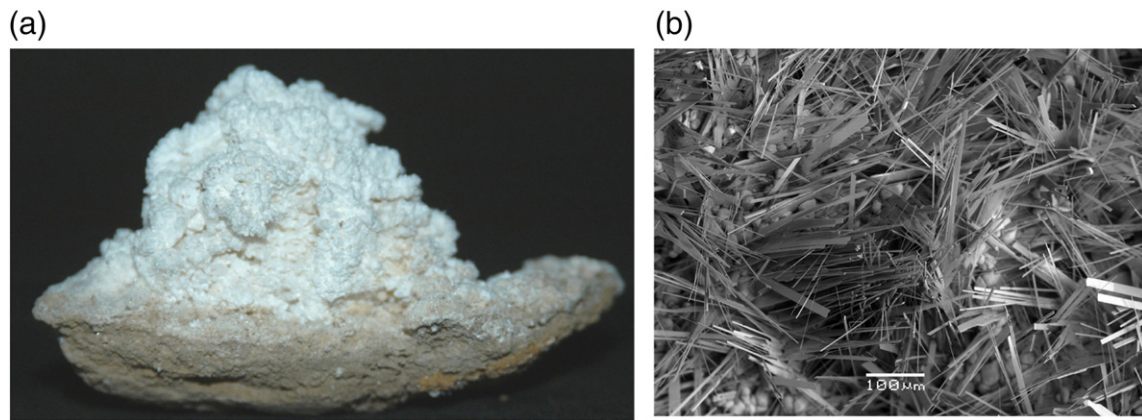
Fig. 31. (a) Side view of fibrous mascagnite efflorescence from F1. Sand substrate is at the bottom. Horizontal field of view is 9 cm. (b) SEM image of bladed mascagnite crystals.

rings and they were overlooked in early sampling campaigns. More rarely nitratine occurs as thin white crusts of delicate branching intergrowths of white to clear 0.05 mm crystals (Fig. 37a) that may be up to 100 μm in thickness (Fig. 37b). Nitratine had been identified as early as 1902 from along the old beach lines of the Salton Sea east of the "Mud Volcanoes" in T.10S. R.14E. (Bailey, 1902).

Ammonium sulfate is a common fertilizer and the process of nitrification, how ammonium is broken down to produce useable nitrate, has been attributed to bacterial action (Praveen-Kumar et al., 1989). In particular *Nitrosomonas* oxidizes ammonia (and ammonium) into nitrite while *Nitrobacter* converts the nitrite to nitrate. Similar moderately

thermophilic nitrifying bacteria (*Nitrosomonas* and *Nitrospira*) have been found associated with hot springs (Lebedeva et al., 2005). They showed that the ammonia- and nitric-oxidizing bacteria were able to be cultured in the temperature ranges of 27°–55 °C and 40°–60 °C, respectively. Ammonia-oxidizing Archea (*Candidatus*, *Crenarchaeota*) have also been found associated with hot springs (Chen et al., 2016; Reigstad et al., 2008).

The location of the brown nitratine-containing deposits infers that ammonium sulfate solutions are diffusing outward from the mascagnite rich central zone. The location of the nitratine zone away from the fumaroles may in part be due to a reduced concentration of ammonium
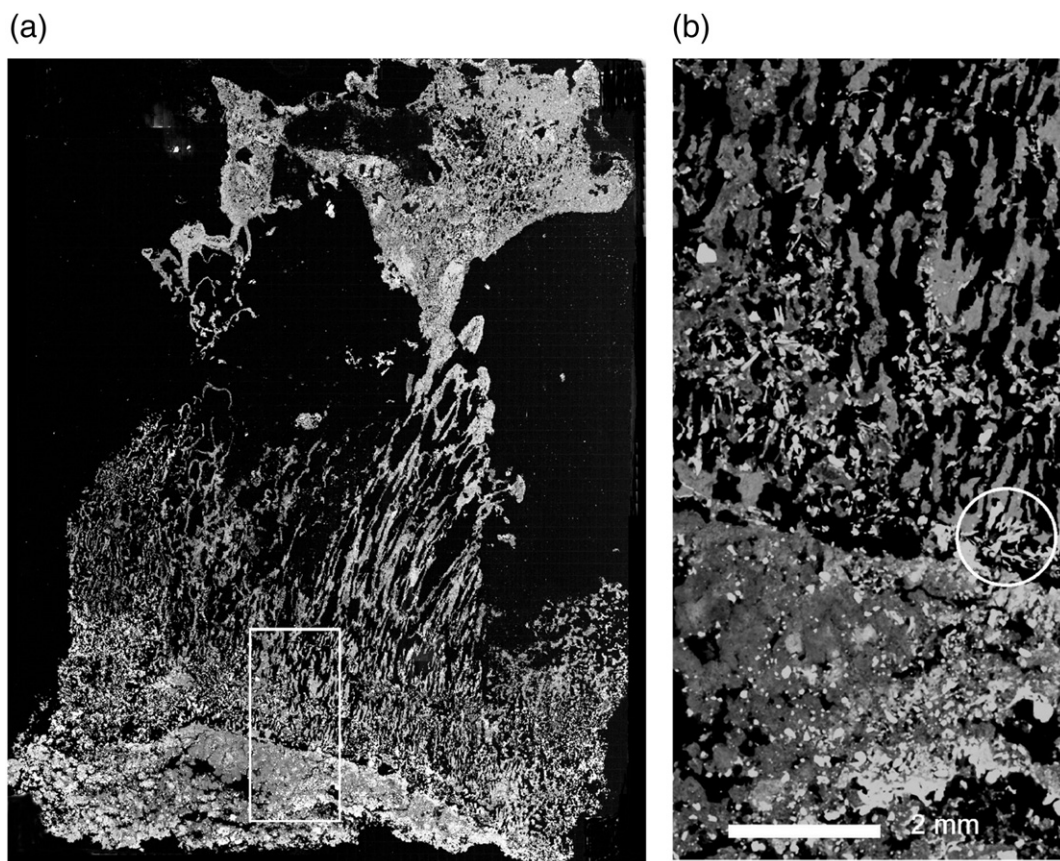

Fig. 32. Backscatter SEM images of a cross section through a fibrous columnar mascagnite growth. (a) Field of view is 4 cm × 6 cm, surface is at top. Base consists of quartz sand cemented by massive mascagnite. Bright grains at bottom are elemental sulfur and sand in a solid mascagnite matrix. (b) Close up of base of mascagnite columns — enlarged view of box in (a). Base of columns include bladed koktaite (bright grains — circled).
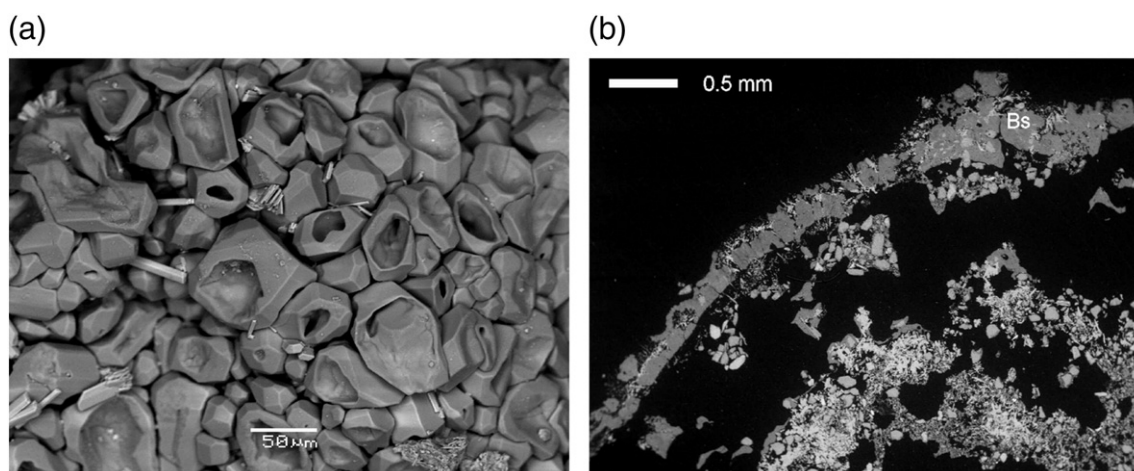
Fig. 33. (a) SEM image of cavernous boussingaultite crystals from F1. (b) Backscatter SEM image of cross section through boussingaultite (Bs) crust from F2. Underlying material is quartz sand and bladed gypsum.

coupled with lower temperatures that are more favorable for microbial activity. The dark brown color of the nitratine rings also suggests that decomposition of vegetation may also contribute to its formation.

5.2.2. Anhydrite $CaSO_4$; Bassanite $2CaSO_4 \cdot H_2O$

Fine grained anhydrite and bassanite are commonly found in loosely consolidated material just beneath the surface in brown nitratine areas (Figs. 11, 37b). This is surprising since the temperature for the transformation of gypsum to anhydrite has been reported to occur between 42 °C and 58 °C (Blount and Dickson, 1973) and the transition zone is a significant distance from the higher temperatures in the fumarole zone where gypsum has been found to occur very close to sulfur producing vents. The fact that anhydrite is subsurface implies that solar heating cannot be responsible for its formation. However, it has been shown that the transformation temperature from gypsum to anhydrite can be much lower (20–30 °C) in highly concentrated NaCl solutions (Blount and Dickson, 1973). It is noted that microbial activity has been implicated in the formation of nitratine in the transition zone. Gunatilaka (1990) describes how halophyte vegetation and a microbial community is associated with the preferential formation of anhydrite over gypsum in a sabkha environment in Kuwait. At that locality cyanobacteria consisting primarily of *Anabaena constricta*, *Spirolina* sp. and *Synechocystis* sp. along with some fungi and halophylic bacteria formed a thin surface

layer (~0.6 cm) overlying a black layer rich in sulfate reducing coccoid bacteria.

5.2.3. Hexahydrite $MgSO_4 \cdot 6H_2O$; Epsomite $MgSO_4 \cdot 7H_2O$

Hexahydrite and epsomite have been found associated with anhydrite and nitratine at F1 where epsomite was a major constituent of a small light gray ring around a 1 m orange patch of boussingaultite.

5.3. Evaporite zone

The evaporite zone comprises those areas adjacent to the transition zone around fumaroles and the brush line along the marsh to the east of the fumaroles. The mineralogy is more typical of that found in arid closed sedimentary basins. Many of the sulfate minerals in this zone (blödite, glauberite, thenardite, mirabilite) are relatively common along the shoreline of the Salton Sea (Buck et al., 2011).

5.3.1. Blödite $Na_2Mg(SO_4)_2 \cdot 4H_2O$

Large areas containing blödite had been identified by remote sensing but ground truth verification was initially elusive. It was finally determined that the blödite was present in small amounts as 2–3 mm granular clusters (micro-snowballs) scattered on the surface at F1 and F2 (Fig. 38a). This morphology is common for sulfates of pedogenic origin (Buck et al., 2006). More rarely it occurs as corroded euhedral
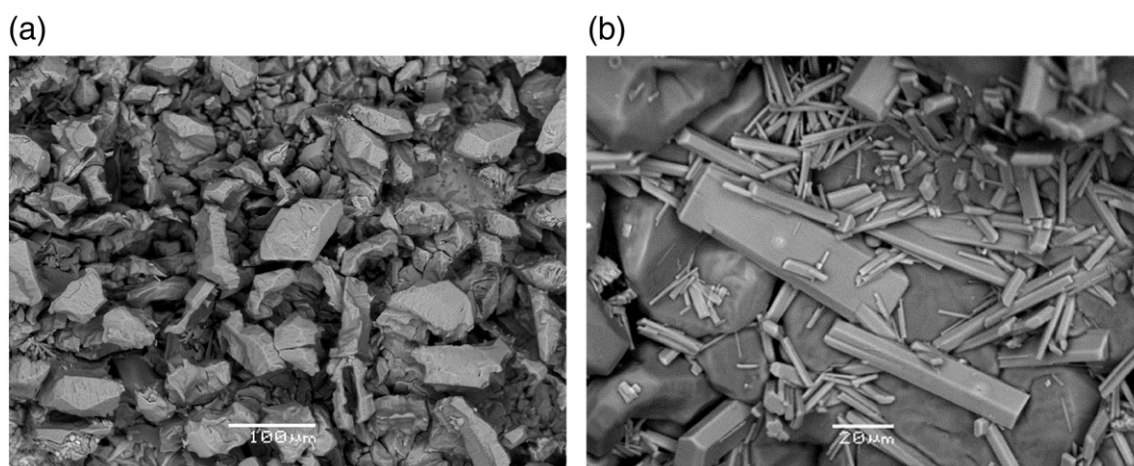

Fig. 34. (a) SEM image of lecontite crystals from F1. (b) SEM image of koktaite crystals on boussingaultite from F1.
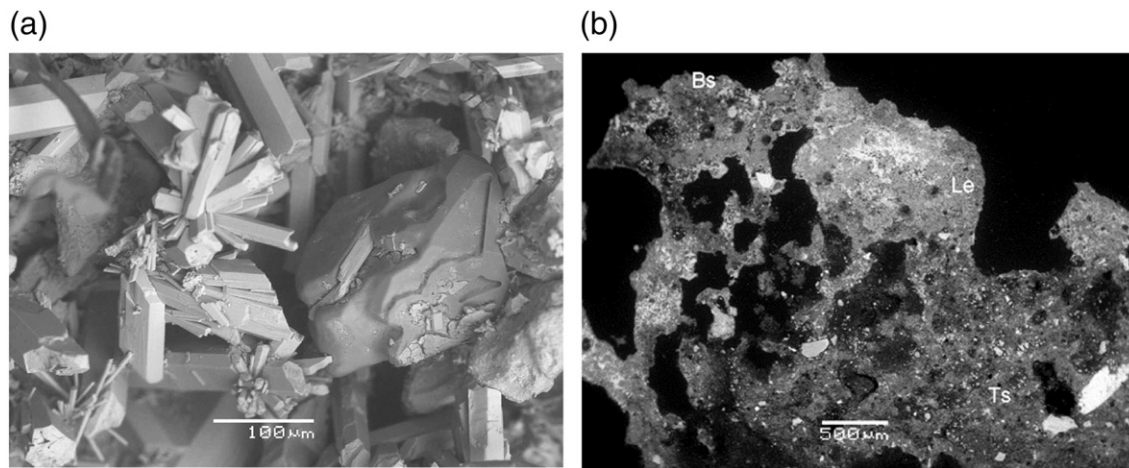
(a)
(b)

Fig. 35. (a) SEM image of blocky tschermigite crystal with bladed gypsum. (b) Backscatter SEM image of cross section of yellow efflorescence from F1. Top zone is a mixture of boussingaultite (Bs), lecontite (Le) and an unidentified Na–K–Fe sulfate (white). Bottom darker zone is tschermigite (Ts).

crystals to 0.3 mm (Fig. 38b). Cross sections of these samples revealed a blödite crust up to 1 mm thick which was underlain by sand that was poorly consolidated with minute (0.05 mm) acicular glauberite (Fig. 39). Blödite has also been mapped (and verified) along the brush line. Blödite crystallizes between -6.2 °C and 21.6 °C from solutions containing its constituent ions. At -6.3 °C it is in equilibrium with epsomite [$MgSO_4 \cdot 7H_2O$] and mirabilite [$Na_2SO_4 \cdot 10H_2O$] and at 21.6 °C with vanthoffite [$MgNa_6(SO_4)_4$] and löweite [$Mg_2Na_4(SO_4)_4 \cdot 5H_2O$] while from solutions saturated in NaCl it may form at temperatures between -15.3 °C and 15.3 °C (Palache et al., 1951).

5.3.2. Konyaite $Na_2Mg(SO_4)_2 \cdot 5H_2O$

On November 28, 2013 botryoidal efflorescent konyaite occurred in growths collected from several centimeter-deep boot prints following a heavy rain that occurred 5 days earlier. On a later trip it formed more extensive deposits at the base of a small gryphon (at F2). Konyaite is relatively unstable and under low humidity conditions alters to blödite (Van Doesburg et al., 1982). However, it has been shown that synthetic konyaite completely decomposes to a mixture of thenardite, hexahydrite, blödite and löweite (Mills et al., 2010).

5.3.3. Glauberite $Na_2Ca(SO_4)_2$

Glauberite was identified by XRD as a minor constituent in areas containing blödite at F1 and F2NC. It occurs as acicular crystals (to 50 μm) in

loosely consolidated material below blödite crusts (Fig. 39b, 40a). It has not been recognized visually.

5.3.4. Thenardite Na_2SO_4

The presence of conspicuous thenardite appears to be ephemeral. About a month after a heavy rain (2.4 cm) on November 23, 2013 extensive crusts of thenardite, often with or after mirabilite (Fig. 40b), were observed on the west side of F2 complex and the F2 SE brush line mud flats. These crusts were not present on previous visits. Isolated patches of thenardite have also been identified from the outer portions of the F2 north complex. Thenardite and blödite have typically been identified by remote sensing along the brush line. It has been difficult to identify in hand samples. A cross section of material from the brush line revealed thenardite intergrown with blödite and minor glauberite (Fig. 41a). In January 2014 extensive regions of halite around F1 were identified as containing minor amounts of thenardite and blödite.

5.3.5. Mirabilite $NaSO_4 \cdot 10H_2O$

The existence of mirabilite is also ephemeral and extensive crusts altering to thenardite were observed in late December 2013 on the west side of the F2 field and along the brush line SE of F2. Bladed crystals of mirabilite, about 4 mm × 20 mm, altering to thenardite were found in deep boot prints and tire tracks at F2 (Fig. 41b). At some point after
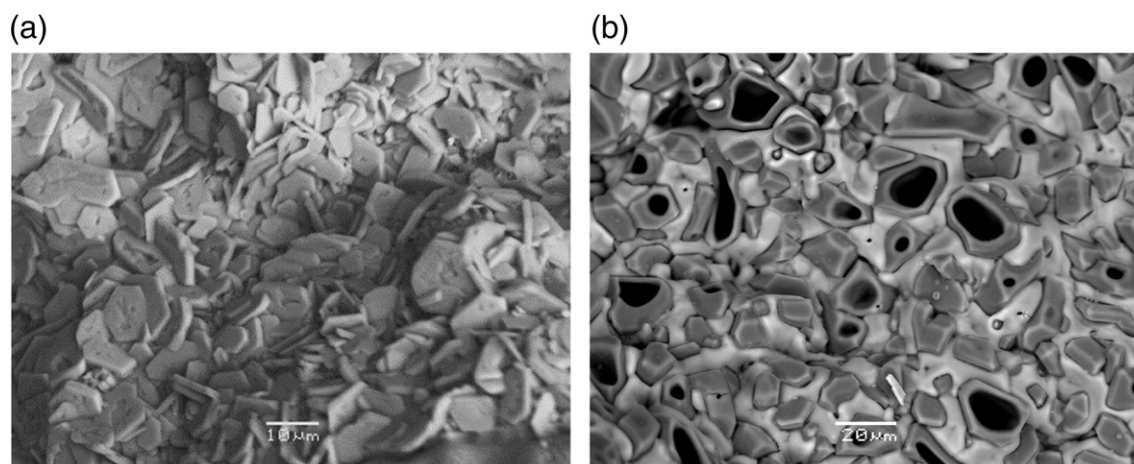
(a)
(b)

Fig. 36. a) SEM image of pseudohexagonal natrojarosite crystals. b) SEM image of cavernous mascagnite surrounded by sal ammoniac from F1.
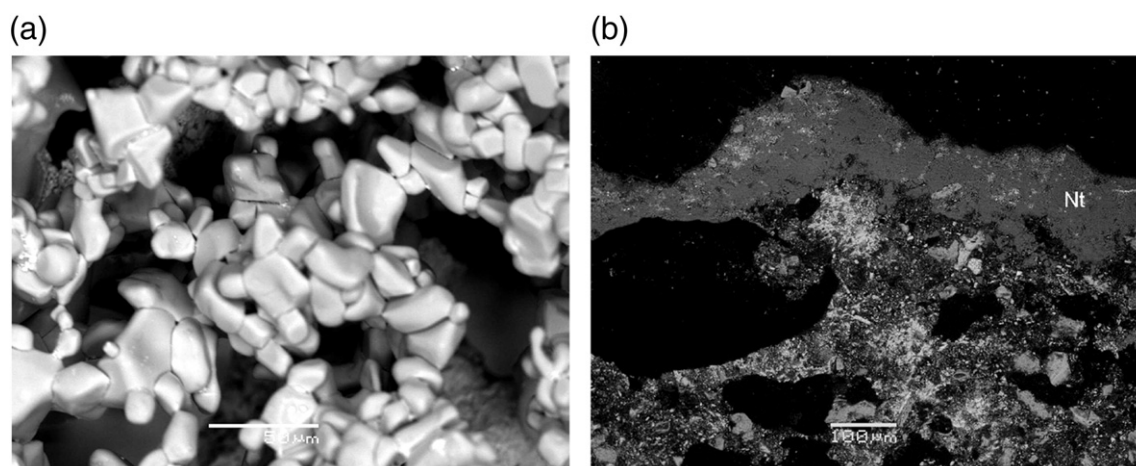
Fig. 37. (a) SEM image of nitratine crystals from F1. (b) Backscatter SEM image of polished cross section of nitratine crust (Nt) from F1. Bright areas under crust are anhydrite/bassanite.

the visit on November 29, 2013 these depressions evidently partially filled with saturated fluids from which the mirabilite crystallized. The thenardite forms pseudomorphic hollow casts after the mirabilite crystals. These casts are very delicate and are probably easily disturbed and redistributed by wind and blowing sand.

5.3.6. Bischofite $MgCl_2 \cdot 6H_2O$

Granular bischofite, associated with acicular glauberite, was found in material collected from the brush line in 2015 that was identified by remote sensing as containing blödite (Fig. 41b).

5.3.7. Halite NaCl

Halite is ubiquitous as thin white surface films and crystalline crusts away from the gryphons and fumaroles. The extent of the halite efflorescence varies depending on how recently it rained and the amount of time to draw saline solutions to the surface from capillary action. Cubic crystals of halite to 3 mm have been observed in boot prints and tire tracks where water accumulated after heavy rains.

6. Comparison with the Davis-Schrimpf fumarole field

The Davis-Schrimpf (DS) fumarole field lies 3.2 km to the southeast on the same trend as the F1 and F2 fields. Since it is further from the Salton Sea it is drier and because the mud has a thicker consistency

much taller gryphons (to 3 m) have developed (Mazzini et al., 2011; Onderdonk et al., 2011). Water dominated seeps have temperatures between 15 °C and 32 °C while mud pots and seeps are hotter (22–62 °C) (Svensen et al., 2007). In contrast many of the clear pools at F1 and the main mud pot area at F2 are boiling, but distal pools at F2 are near ambient. The water from DS has pH that varies from 5.2 to 6.8 and the salinity (total dissolved solids) ranges from 1.5 to 134 g/l (Svensen et al., 2007, 2009; Mazzini et al., 2011). These are comparable with what has been observed at F1 and F2, but from limited measurements, the maximum TDS content at F2 was 87 g/l. Significant ammonia emissions have been mapped at F1 and F2 (Tratt et al., 2011) but the exact gas composition has not been determined. No ammonia has been detected from the fumaroles at DS where the main gaseous species are carbon dioxide and to a much lesser extent — methane (<2 vol.%) (Svensen et al., 2007; Mazzini et al., 2011). It is not surprising that no ammonium-containing minerals have been identified at DS. There appears to be a much deeper source of ammonia at DS since it has been observed in the cooling tower emissions from the adjacent geothermal power plant (Tratt et al., 2016). The most obvious difference between DS and F1–F2 is related to the ammonia emissions in the latter which are responsible for the significant development of ammonium-containing sulfates (mascagnite, boussingaultite, lecontite and koktaite). Sulfates at DS are poorly developed and limited to a ~20 cm diameter area at the summit of a small (1 m high) gryphon at the
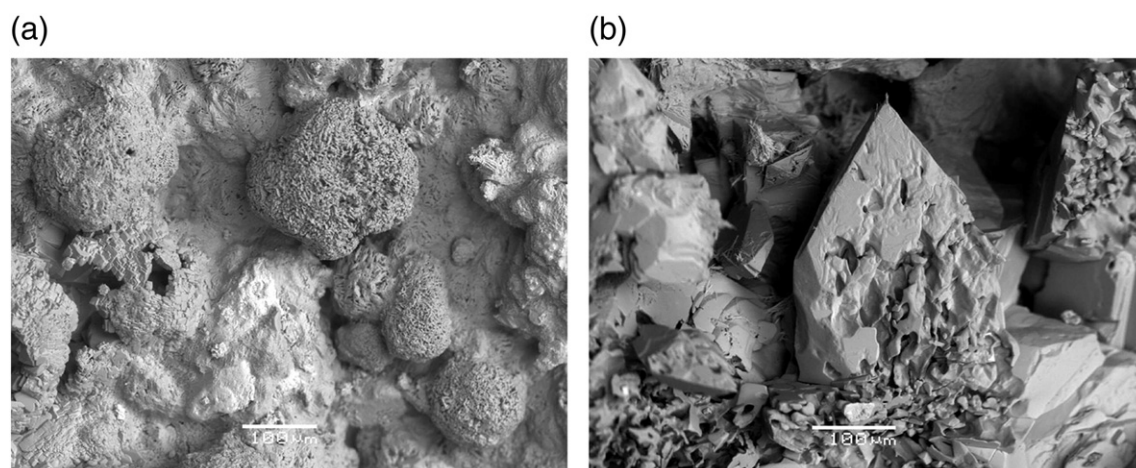

Fig. 38. (a) SEM image of clusters of blödite micro-snowballs from F2. (b) Corroded blödite crystal from F2.
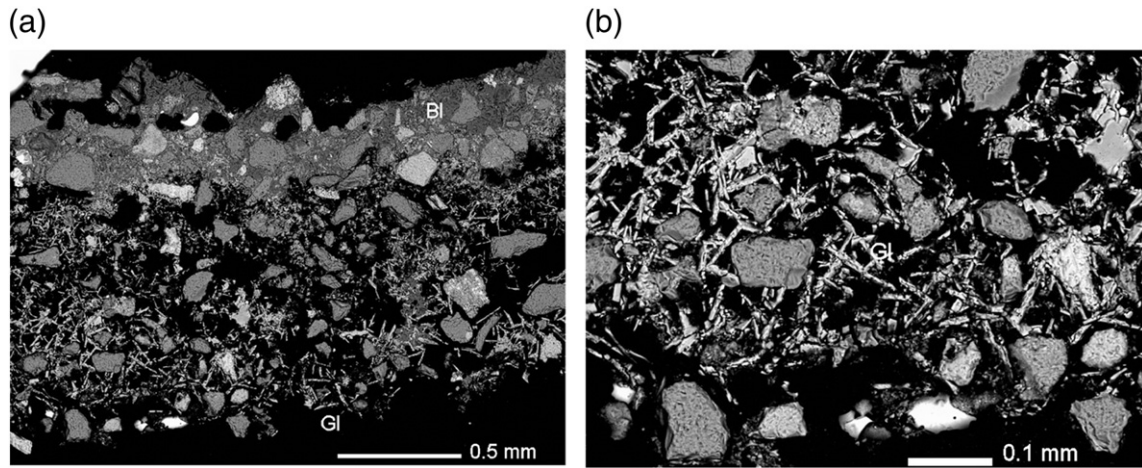
Fig. 39. (a) Backscatter SEM cross section through surface blödite (Bl) crust (top). (b) Close up of poorly consolidated sand under blödite crust with acicular grains of glauberite (Gl).
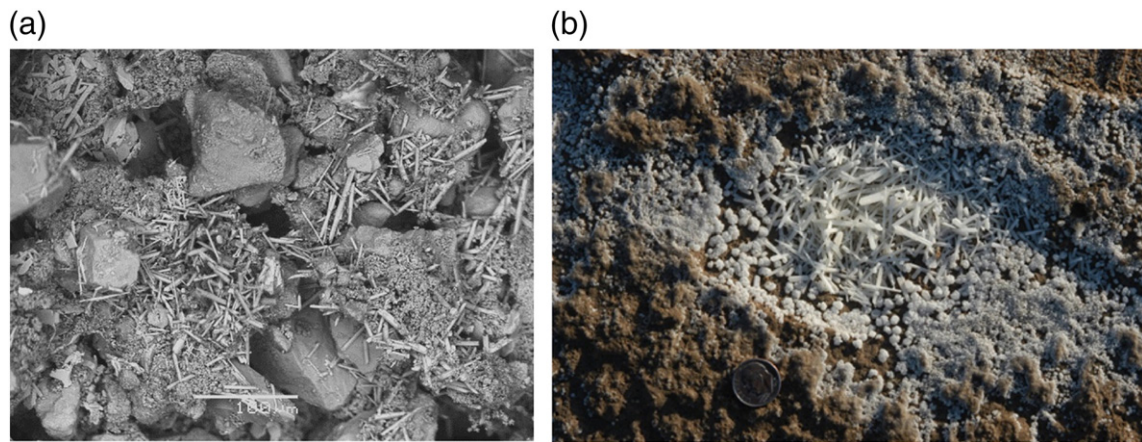

Fig. 40. (a) SEM image of acicular glauberite crystals on sand grains below crust of blödite from F2. (b) Thenardite after mirabilite precipitated from solution collected in a boot print. FOV 15 cm.

south side of the field and two nearby surface patches (to 3 m × 3 m). Mazzini et al. (2011) trenched one of the surface exposures and found tamarugite and blödite. Adams and Lynch (2014) performed a more extensive study and additionally found limited quantities of hexahydrite, starkeyite, epsomite, gypsum, anhydrite, pickeringite, halotrichite, natrojarosite, alum-K, thenardite, voltaite, cinnabar and sulfur. Reath and Ramsey (2013) mapped extensive fields of anhydrite, gypsum and their unknown Mg-sulfate at DS. We were unable to corroborate this latter observation, which we believe may be interpreted differently as discussed in Section 4.2.4.
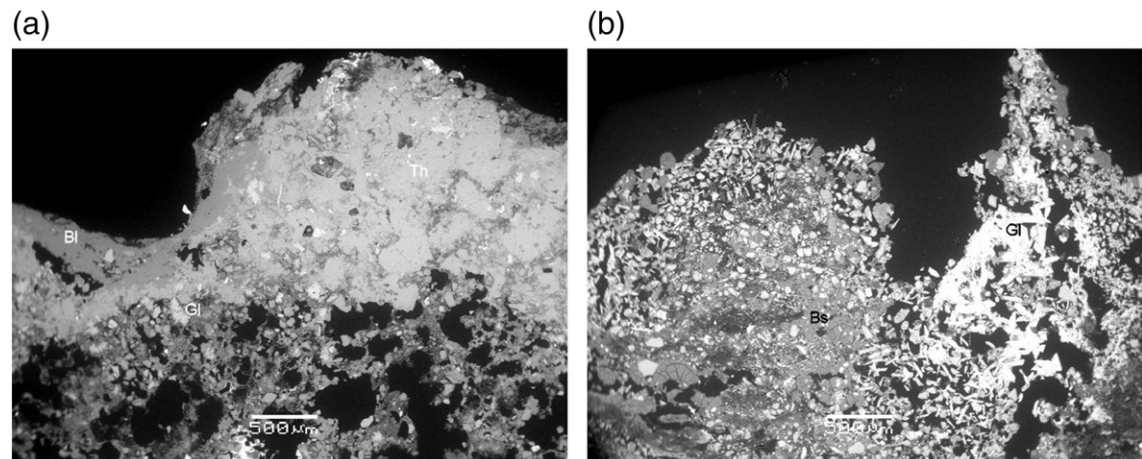

Fig. 41. a) Backscatter SEM image of a cross section of thenardite (Th)–blödite (Bl)–glauberite (Gl) crust from the brush line area. The glauberite forms small (200–300 μm) radiating clusters of crystals. b) Backscatter SEM image of cross section of bischofite (Bs) and acicular glauberite (Gl).

Table 6
Summary of major surface and subsurface mineralogy of fumarole zones.

	Fumarole zone	Transition zone	Evaporite zone
Surface	Mascagnite, boussingaultite, gypsum, lecontite, koktaite, sulfur[a]	Nitratine	Blödite, thenardite, mirabilite, halite
Sub-surface[b]	Quartz, sulfur	Quartz, anhydrite, bassanite	Quartz, glauberite

[a] Localized to active vents.
[b] Based on limited sampling.

7. Summary/conclusions

We have described an active moderate-temperature ammonia-emitting fumarole area which has an unusual assemblage of ammonium sulfate minerals that formed following the drop in the Salton Sea level from 2009 to 2017. This study is significant since recently access to the area has been restricted and there have been large scale changes to the landscape and hydrology as a result of wind-borne dust mitigation efforts. Plans for a large scale geothermal plant on the site further endanger the long term fate of the fumaroles.

The large scale mineral zonation mapped by SEBASS and Mako was verified by ground truth sampling. The zonation has been sustained and relatively consistent since about 2013 when the fumaroles had become fully emerged and relatively dry. Recently this trend has been reversed for F1 which now is surrounded by shallow water and much of the evaporite and transition zone has been resubmerged. Minor variations in mineralogy are probably a result of differences in rainfall which can dissolve and transport highly soluble salts (Table 5), ground water level (a function of Salton Sea level and irrigation runoff) and recent daytime temperatures. The latter two may influence the level of the capillary fringe and the formation of evaporative crusts. Other factors such as wind and wind-blown sand may also modify the surface mineralogy by sandblasting, transport or burial. The large scale mineral rings also reproduce the much smaller zonation seen around individual satellite fumarole vents (Fig. 11). In these cases sulfur crystals are found surrounding the vents, usually in close association with gypsum. Outwardly there is a zone closely associated with the fumaroles consisting of ammonium sulfates (mascagnite, lecontite, koktaite and boussingaultite) followed by a transition zone containing a dark brown zone of nitratine and subsurface anhydrite/bassanite (Table 6). The outermost zone is more related to evaporites. This zone with blödite, and to a lesser extent thenardite, is usually not observed around smaller vents. An example of the small scale zonation is shown in Fig. 28, which was constructed from diffuse reflectance FTIR spectra obtained with the Exoscan.

The mineral zonation may be a result of chemical and temperature gradients from the ammonia emitting vents and mineral solubilities probably also contribute. In the evaporation of complex salt mixtures from hypersaline lakes, typically the least soluble minerals sequentially precipitate first and form the outer-most rings of the concentric structures (Hardie, 1968; Hunt et al., 1966; Jones, 1965). At the fumaroles gypsum is usually associated with sulfur closest to the vents and it along with anhydrite are the least soluble sulfates present. The ammonium sulfates mascagnite, boussingaultite and lecontite are closely associated with the vents but are much more water soluble and form thick efflorescent growths on the surface. Surrounding this ammonium dominated fumarole zone is a transition region where nitrates form from the ammonium salts, probably assisted by microbial action. This is characterized by a dark brown zone which contains nitratine at the surface. Outward from this is a less recognizable zone with sulfate minerals (blödite, thenardite) more representative of the end stage of evaporite sequences from neutral brines such as in the Saline Valley, CA (Hardie, 1968) or pedogenic soils in arid environments (Buck et al., 2006). In the latter case the sulfates form a surface crust resulting from high evaporation rates along the top of the capillary fringe. Blödite, thenardite and glauberite are relatively common along the shoreline of the Salton Sea (Buck et al., 2011), and other dry saline lakes (Mees et al., 2011; Orti et al., 2002).

One of the significant findings of this study is field and remote sensing verification that fine grained quartz or other silicates entrapped in halite can produce unexpected modifications to the reflectance/emissivity spectra of underlying minerals, in this case to quartz, in the outer evaporite zone. The result is a range of spectra that do not resemble end member spectra in remote sensing spectral libraries. This greatly complicates the correct identification and mapping of these areas and points to the importance of performing ground truth sampling of such halite-rich areas.

References

Adams, P.M., Lynch, D.K., 2014. A mineralogical inventory of geothermal features southeast of the Salton Sea, Imperial County, California. In: Reynolds, R. (Ed.), 2014 Desert Symposium Field Guide and Proceedings. Cal. State Univ. Fullerton Desert Studies Consortium:pp. 100–111 (http://nsm.fullerton.edu/dsc/images/DSCdocs/2014Notadroplefttodrink.pdf#page=100.).

Bailey, G.E., 1902. The saline deposits of California. Calif. State Min. Bur. Rpt. 24, 178–180.

Baldridge, A.M., Hook, S.J., Grove, C.I., Rivera, G., 2009. The ASTER spectral library version 2.0. Remote Sens. Environ. 113 (4):711–715. https://doi.org/10.1016/j.rse.2008.11.007.

Berger, J.A., King, P.L., Green, A., Craig, M.A., Spilde, M.N., Wright, S.P., Kunkel, T.S., Lee, Rachel J., 2015. Effect of halite coatings on thermal infrared spectra. J. Geophys. Res. Solid Earth 120:2162–2178. https://doi.org/10.1002/2014JB011712.

Bishop, H.K., Bricarello, J.R., 1978. Scaling and corrosion in an experimental geothermal power plant. J. Pet. Technol. 30 (9):1240–1242. https://doi.org/10.2118/6612-PA.

Blount, C.W., Dickson, F.W., 1973. Gypsum-anhydrite equilibria in the systems CaSO$_4$-H$_2$O and CaCO$_4$-NaCl-H$_2$O. Am. Mineral. 58, 323–331.

Brothers, D., Driscoll, N., Kent, G., Harding, A., Babcock, J., Baskin, R., 2009. Tectonic evolution of the Salton Sea inferred from seismic reflection data. Nat. Geosci. 2:581–584. https://doi.org/10.1038/ngeo590.

Buck, B.J., Wolff, K., Merkler, D.J., McMillan, N.J., 2006. Salt mineralogy of Las Vegas Wash, Nevada: morphology and subsurface evaporation. Soil Sci. Soc. Am. J. 70 (5): 1639–1651. https://doi.org/10.2136/sssaj2005.0276.

Buck, B.J., King, J., Etyemezian, V., 2011. Effects of salt mineralogy on dust emissions, Salton Sea, California. Soil Sci. Soc. Am. J. 75 (5):1958–1971. https://doi.org/10.2136/sssaj2011.0049.

Buckland, K.N., Young, S.J., Keim, E.R., Johnson, B.R., Johnson, P.D., Tratt, D.M., 2017. Tracking and quantification of gaseous chemical plumes from anthropogenic emission sources within the Los Angeles Basin. Remote Sens. Environ. 201:275–296. https://doi.org/10.1016/j.rse.2017.09.012.

Chen, S., Peng, X., Xu, H., Ta, K., 2016. Nitrification of archaeal ammonia oxidizers in a high-temperature hot spring. Biogeosciences 13 (7):2051–2060. https://doi.org/10.5194/bg-13-2051-2016.

Chou, I.-M., Seal II, R.R., Wang, A., 2013. The stability of sulfate and hydrated sulfate minerals near ambient conditions and their significance in environmental and planetary sciences. J. Asian Earth Sci. 62:734–758. https://doi.org/10.1016/j.jseaes.2012.11.027.

Christensen, P.R., Bandfield, J.L., Hamilton, V.E., Howard, D.A., Lane, M.D., Piatek, J.L., Ruff, S.W., Stefanov, W.L., 2000. A thermal emission spectral library of rock-forming minerals. J. Geophys. Res. 105 (E4):9735–9739. https://doi.org/10.1029/1998JE000624.

Ciesielczuk, J., Zaba, J., Bzowska, G., Gaidzik, K., Glogowska, M., 2013. Sulphate efflorescences at the geyser near Pinchollo, southern Peru. J. S. Am. Earth Sci. 42, 186–193.

Clark, R.N., Swayze, G.A., Wise, R., Livo, K.E., Hoefen, T.M., Kokaly, R.F., Sutley, S.J., 2007. USGS Digital Spectral Library splib06a. U.S. Geological Survey, Data Series 231 (http://speclab.cr.usgs.gov/spectral.lib06/ds231/datatable.html).

Cluotis, E.A., Hawthorne, F.C., Mertzman, S.A., Krenn, K., Craig, M.A., Marcino, D., Methot, M., Strong, J., Mustard, J.F., Blaney, D.L., Bell III, J.F., Vilas, F., 2006. Detection and discrimination of sulfate minerals using reflectance spectroscopy. Icarus 184 (1): 121–157. https://doi.org/10.1016/j.icarus.2006.04.003.

Corazza, E., Sabelli, C., Giuseppetti, G., 1967. The crystal structure of lecontite, $NaNH_4SO_4 \cdot 2H_2O$. Acta Cryst. 22:683–687. https://doi.org/10.1107/S0365110X67001355.

Dangermond, J., 2003. Salton Sea Atlas. ESRI Press (136 pp.).

DeMartln, C., Gramaccolli, C.M., Campostrini, I., 2009. Brontesite, $(NH_4)_3PbCl_5$, a new product of fumarolic activity from La Fossa crater, Aeolian Islands, Italy. Can. Mineral. 47 (5):1237–1243. https://doi.org/10.3749/canmin.47.5.1237.

Dimitrov, L., 2002. Mud volcanoes—the most important pathway for degassing deeply buried sediments. Earth-Sci. Rev. 59 (1–4):49–76. https://doi.org/10.1016/S0012-8252(02)00069-7.

Draper, N.R., Smith, H., 1998. Applied regression analysis. Wiley Series in Probability and Statistics, 3rd edition.

Dunning, G.E., Cooper Jr., J.F., 1993. History and minerals of The Geysers, Sonoma County, California. Mineral. Rec. 24 (5), 339–354.

Eastes, J.W., 1989. Spectral properties of halite-rich mineral mixtures: Implications for remote sensing of highly saline environments. Remote Sens. Environ. 27:289–304. https://doi.org/10.1016/0034-4257(89)90089-8.

Faust, R.J., Bloss, D.F., 1963. X-ray study of lecontite. Am. Mineral. 48 (1–2):180–188 (http://www.minsocam.org/ammin/AM48/AM48_180.pdf).

Fuller, M.P., Griffiths, P.R., 1978. Diffuse reflectance measurements by infrared Fourier transform spectrometry. Anal. Chem. 50 (13):1906–1910. https://doi.org/10.1021/ac50035a045.

Gunatilaka, A., 1990. Anhydrite diagenesis in a vegetated sabkha, Al-Khiran, Kuwait, Arabian Gulf. Sedimentary Geology 69:95–116. https://doi.org/10.1016/0037-0738(90)90103-Z.

Gurbuz, A., 2010. Geometric characteristics of pull-apart basins. Lithosphere 2 (3): 199–206. https://doi.org/10.1130/L36.1.

Hackwell, J.A., Warren, D.W., Bongiovi, R.P., Hansel, S.J., Hayhurst, T.L., Mabry, D.J., Sivjee, M.G., Skinner, J.W., 1996. LWIR/MWIR imaging hyperspectral sensor for airborne and ground-based remote sensing. Proc. SPIE 2819:102–107. https://doi.org/10.1117/12.258057.

Hall, J.L., Boucher, R.H., Gutierrez, D.J., Hansel, S.J., Kasper, B.P., Keim, E.R., Moreno, N.M., Polak, M.L., Sivjee, M.G., Tratt, D.M., Warren, D.W., 2011. First flights of a new airborne thermal infrared imaging spectrometer with high area coverage. Proc. SPIE 8012:801203. https://doi.org/10.1117/12.884865.

Hanks, H.G., 1882. Mud volcanoes and the Colorado Desert. Second annual report of the State Mineralogist of California; from December 1, 1880 to October 1, 1882. Calif. Min. Bur. Rep. 2, 227–240.

Hardie, L.A., 1968. The origin of the recent non-marine evaporite deposit of Saline Valley, Inyo County, California. Geochim. Cosmochim. Acta 32 (12):1279–1301. https://doi.org/10.1016/0016-7037(68)90029-X.

Hauksson, E., Stock, J., Hutton, K., Yang, W., Vidal-Villegas, A., 2011. The 2010 M_w 7.2 El Mayor-Cucapah earthquake sequence, Baja California, Mexico and Southernmost California, USA: active seismotectonics along the Mexican Pacific Margin. Pure Appl. Geophys. 168 (8):1255–1277. https://doi.org/10.1007/s00024-010-0209-7.

Helgeson, H., 1968. Geologic and thermodynamic characteristics of the Salton Sea geothermal system. Am. J. Sci. 266 (3):129–166. https://doi.org/10.2475/ajs.266.3.129.

Hunt, G.R., Vincent, R.K., 1968. The behavior of spectral features in the infrared emission from particulate surfaces and various grain size. J. Geophys. Res. 73:6039–6046. https://doi.org/10.1029/JB073i018p06039.

Hunt, C.B., Robinson, T.W., Bowles, W.A., Washburn, A.I., 1966. Hydrologic Basin, Death Valley, California. USGS Prof. Paper 494B (https://pubs.usgs.gov/pp/0494b/report.pdf).

The Salton Sea Centennial Symposium. In: Hurlbert, S.H. (Ed.), Proceedings of a Symposium Celebrating a Century of Symbiosis Among Agriculture, Wildlife and People, 1905–2005, Held in San Diego, California, USA, March 2005 (Reprinted from Hydrobiologia 604 (1). http://rd.springer.com/journal/10750/604/1/page/1).

Jones, B.F., 1965. Hydrology and mineralogy of Deep Springs Lake, Inyo County California. USGS Prof. Paper 502A (https://pubs.usgs.gov/pp/0502a/report.pdf).

Kennan, G., 1917. The Salton Sea: An Account of Harriman's Fight with the Colorado River. The MacMillan Company, New York (106 pp.).

Kim, J., Kim, S., Tazaki, K., 2002. Mineralogical characterization of microbial ferrihydrite and schwertmannite, and non-biogenic Al-sulfate precipitates from acid mine drainage in the Donghae mine area, Korea. Environ. Geol. 42 (1):19–31. https://doi.org/10.1007/s00254-002-0530-2.

Kirkland, L., Herr, K., Keim, E., Adams, P., Salisbury, J., Hackwell, J., Treiman, A., 2002. First use of an airborne thermal infrared hyperspectral scanner for compositional mapping. Remote Sens. Environ. 80 (3):447–459. https://doi.org/10.1016/S0034-4257(01)00323-6.

Kirkland, L.E., Herr, K.C., Adams, P.M., 2003. Infrared stealthy surfaces: why TES and THEMIS may miss some substantial mineral deposits on Mars and implications for remote sensing of planetary surfaces. J. Geophys. Res. 108 (E12):5137. https://doi.org/10.1029/2003JE002105.

Koenig, J.B., 1969. Geysers geothermal field. Calif. Div. Mines, Geol., Mineral Info. Serv. 22 (8), 123–128.

Krohn, M.D., Kendall, C., Evans, J.R., Fries, T.L., 1993. Relations of ammonium minerals at several hydrothermal systems in the western US. J. Volcanol. Geotherm. Res. 56 (4):401–413. https://doi.org/10.1016/0377-0273(93)90005-C.

Lachenbruch, A., Sass, J., Galanis, S., 1985. Heat flow in southernmost California and the origin of the Salton Trough. J. Geophys. Res. 90 (B8):6709–6736. https://doi.org/10.1029/JB090iB08p06709.

Lane, M.D., 2007. Mid-infrared emission spectroscopy of sulfate and sulfate-bearing minerals. Am. Mineral. 92:1–18. https://doi.org/10.2138/am.2007.2170.

Lapham, D.M., Barnes, J.H., Downey Jr., W.F., Finkelman, R.B., 1980. Mineralogy Associated with Burning Anthracite Deposits of Eastern Pennsylvania. vol. 78. Commonwealth of Pennsylvania, Department of Environmental Resources, Bureau of Topographic and Geologic Survey (https://ia801907.us.archive.org/5/items/mineralogyassoci00laph/mineralogyassoci00laph.pdf).

Lebedeva, E.V., Alawi, M., Fiencke, C., Namsaraev, B., Bock, E., Spieck, E., 2005. Moderately thermophilic nitrifying bacteria from a hot spring of the Baikal rift zone. FEMS Microbiol. Ecol. 54 (2):297–306. https://doi.org/10.1016/j.femsec.2005.04.010.

LeConte, J.L., 1855. Account of some volcanic springs in the desert of the Colorado, Southern California. Am. J. Sci. Arts (2nd Ser.) 19 (55), 1–6.

Lee, T.C., Cohen, L.H., 1979. Onshore and offshore measurements of temperature gradients in the Salton Sea geothermal area, California. Geophysics 44 (2):206–215. https://doi.org/10.1190/1.1440962.

Lonsdale, P., 1989. Geology and tectonic history of the Gulf of California. In: Winterer, E.L., Hussong, D.M., Decker, R.W. (Eds.), The Eastern Pacific Ocean and Hawaii. Geological Society of America, The Geology of North America, N:pp. 499–521 https://doi.org/10.1130/dnag-gna-n.499.

Lynch, D.K., 2011. The coming land bridge to Mullet Island. In: Reynolds, R. (Ed.), 2011 Desert Symposium Field Guide and Proceedings. Cal. State Univ. Fullerton Desert Studies Consortium:pp. 96–100 (http://nsm.fullerton.edu/dsc/images/DSCdocs/2011shrinkingpliocene.pdf#page=97).

Lynch, D.K., Adams, P.M., 2014. Hot volcanic vents on Red Island, Imperial County, California. In: Reynolds, R. (Ed.), 2014 Desert Symposium Field Guide and Proceedings. Cal. State Univ. Fullerton Desert Studies Consortium:pp. 117–120 (http://nsm.fullerton.edu/dsc/images/DSCdocs/2014Notadroplefttodrink.pdf#page=117).

Lynch, D.K., Hudnut, K.W., 2008. The Wister mud pot lineament: southeastward extension or abandoned strand of the San Andreas Fault? Bull. Seismol. Soc. Am. 98 (4):1720–1729. https://doi.org/10.1785/0120070252.

Lynch, D.K., Hudnut, K.W., Adams, P.M., 2013. Development and growth of recently-exposed fumarole fields near Mullet Island, Imperial County, California. Geomorphology 195:27–44. https://doi.org/10.1016/j.geomorph.2013.04.022.

Lynch, D.K., Adams, P.M., Tratt, D.M., 2014. Mullet Island has become a peninsula. In: Reynolds, R. (Ed.), 2014 Desert Symposium Field Guide and Proceedings. Cal. State Univ. Fullerton Desert Studies Consortium:pp. 113–116 (http://nsm.fullerton.edu/dsc/images/DSCdocs/2014Notadroplefttodrink.pdf#page=113).

Macdonald, K.C., 1982. Mid-ocean ridges: fine scale tectonic, volcanic and hydrothermal processes within the plate boundary zone. Annu. Rev. Earth Planet. Sci. 10: 155–190. https://doi.org/10.1146/annurev.ea.10.050182.001103.

Manga, M., Brumm, M., Rudolph, M., 2009. Earthquake triggering of mud volcanoes. Mar. Pet. Geol. 26 (9):1785–1798. https://doi.org/10.1016/j.marpetgeo.2009.01.019.

Manolakis, D., Marden, D., Shaw, G.A., 2003. Hyperspectral image processing for automated target detection applications. Lincoln Lab. J. 14 (1): 79–116 (http://www.ll.mit.edu/publications/journal/pdf/vol14_no1/14_1hyperspectralprocessing.pdf).

Masalehdani, M.N.-N., Mees, F., Dubois, M., Coquinot, Y., Potdevin, J.-L., Fialin, M., Blanc-Valleron, M.-M., 2009. Condensate minerals from a burning coal-waste heap in Avion, northern France. Can. Mineral. 47 (3):865–884. https://doi.org/10.3749/canmin.47.3.573.

Mazzini, A., Svensen, H., Etiope, G., Onderdonk, N., Banks, D., 2011. Fluid origin, gas fluxes and plumbing system in the sediment-hosted Salton Sea geothermal system (California, USA). J. Volcanol. Geotherm. Res. 205 (3–4):67–83. https://doi.org/10.1016/j.jvolgeores.2011.05.008.

McCauley, C.A., O'Sullivan, A.D., Milke, M.K., Weber, P.A., Trumm, D.A., 2009. Sulfate and metal removal in bioreactors treating acid mine drainage dominated with iron and aluminum. Water Res. 43 (4):961–970. https://doi.org/10.1016/j.watres.2008.11.029.

McKibben, M.A., 2008. The Salton Sea geothermal brines. In: Reynolds, R. (Ed.), 2008 Desert Symposium Field Guide and Proceedings. Cal. State Univ. Fullerton Desert Studies Consortium:pp. 102–106 (http://nsm.fullerton.edu/dsc/images/DSCdocs/2008troughtotrough.pdf#page=102).

Mees, F., Castañeda, C., Herrero, J., Van Ranst, E., 2011. Blödite sedimentation in a seasonally dry saline lake (Salada Mediana, Spain). Sediment. Geol. 238 (1–2):106–115. https://doi.org/10.1016/j.sedgeo.2011.04.006.

Meltzner, A.J., Rockwell, T.K., Owen, L.A., 2006. Recent and long-term behavior of the Brawley fault zone, Imperial Valley, California: an escalation in slip rate? Bull. Seismol. Soc. Am. 96 (6):2304–2328. https://doi.org/10.1785/0120050233.

Mills, S.J., Wilson, S.A., Dipple, G.M., Raudsepp, M., 2010. The decomposition of konyaite: importance in CO_2 in mine tailings. Mineral. Mag. 74:903–917. https://doi.org/10.1180/minmag.2010.074.5.903.

Muffler, L.J.P., White, D.E., 1968. Origin of CO_2 in the Salton Sea geothermal system, southeastern California, USA. Proc. 23rd Intl. Geol. Congress 97, 185–194.

Muffler, L.J.P., White, D.E., 1969. Active metamorphism of the upper Cenozoic sediments in the Salton Sea geothermal field and the Salton Trough, southern California. Geol. Soc. Am. Bull. 80 (2):157–182. https://doi.org/10.1130/0016-7606(1969)80[157:AMOUCS]2.0.CO;2.

Mustard, J.F., Hays, J.E., 1997. Effects of hyperfine particles on reflectance spectra from 0.3 to 25 μm. Icarus 125:145–163. https://doi.org/10.1006/icar.1996.5583.

National Weather Service, 2017. Advanced Hydrologic Prediction Service. http://water.weather.gov/precip/.

Newark, R., Kasmeyer, P., Younker, L., 1988. Shallow drilling in the Salton Sea region: the thermal anomaly. J. Geophys. Res. 93 (B11):13005–13023. https://doi.org/10.1029/JB093iB11p13005.

Onderdonk, N., Shafer, L., Mazzini, A., Svensen, H., 2011. Controls on the expression and evolution of gryphons, mud pots, and caldera features at hydrothermal seeps in the Salton Sea Geothermal Field, Southern California. Geomorphology 130 (3–4): 327–342. https://doi.org/10.1016/j.geomorph.2011.04.014.

Orti, F., Gundogan, I., Helvaci, C., 2002. Sodium sulphate deposits of Neogene age: the Kirmir Formation, Beypazari Basin, Turkey. Sediment. Geol. 146 (3–4):305–333. https://doi.org/10.1016/S0037-0738(01)00140-3.

Palache, C., Berman, H., Frondel, C., 1951. The System of Mineralogy. 7th edition. John Wiley, New York, pp. 449–450.

Parafiniuk, J., Kruszewski, L., 2010. Ammonium minerals from burning coal-dumps of the Upper Silesian Coal Basin (Poland). Geol. Q. 53:341–356 (https://gq.pgi.gov.pl/gq/article/viewFile/7524/6174).

Praveen-Kumar, Aggarwal, R.K., Sharma, B.M., 1989. Nitrification and nitrate movement from ammonium sulphate and urea in sandy soils as affected by their previous applications. Fertil. Res. 21 (1):29–36. https://doi.org/10.1007/BF01054733.

Ramsey, M.S., Christensen, P.R., 1998. Mineral abundance determination: quantitative deconvolution of thermal emission spectra. J. Geophys. Res. 103B:577–596. https://doi.org/10.1029/97JB02784.

Reath, K.A., Ramsey, M.S., 2013. Exploration of geothermal systems using hyperspectral thermal infrared remote sensing. J. Volcanol. Geotherm. Res. 265:27–38. https://doi.org/10.1016/j.jvolgeores.2013.08.007.

Reigstad, L.J., Richter, A., Daims, H., Urich, T., Schwark, L., Schleper, C., 2008. Nitrification in terrestrial hot springs of Iceland and Kamchatka. FEMS Microbiol. Ecol. 64 (2): 167–174. https://doi.org/10.1111/j.1574-6941.2008.00466.x.

Ribeiro da Luz, B., Crowley, J.K., 2010. Identification of plant species by using high spatial and spectral resolution thermal infrared (8.0–13.5 μm) imagery. Remote Sens. Environ. 114 (2):404–413. https://doi.org/10.1016/j.rse.2009.09.019.

Robinson, T.W., Hunt, C.B., 1961. Some extremes of climate in Death Valley, California. Short Papers in the Geologic and Hydrologic Sciences, Articles 1–146: Geological Survey Research 1961. U. S. Geological Survey Prof. Paper 424-B, pp. 192–194.

Robinson, P.T., Elders, W.A., Muffler, L.J., 1976. Quaternary volcanism in the Salton Sea geothermal field, Imperial Valley, California. Geol. Soc. Am. Bull. 87 (3):347–360. https://doi.org/10.1130/0016-7606(1976)87<347:QVITSS>2.0.CO;2.

Ross, C.P., Yates, R.G., 1942. The Coso quicksilver district, Inyo County, California. USGS Bull. 936-Q:394–415 (https://pubs.usgs.gov/bul/0936q/report.pdf).

Rudolph, M.L., Manga, M., 2010. Mud volcano response to the 4 April 2010 El Mayor–Cucapah earthquake. J. Geophys. Res. 115 (B12), B12211. https://doi.org/10.1029/2010JB007737.

Salisbury, J.W., Wald, A., 1992. The role of volume scattering in reducing spectral contrast of reststrahlen bands in spectra of powdered minerals. Icarus 96:121–128. https://doi.org/10.1016/0019-1035(92)90009-V.

Salisbury, J.W., Wald, A., D'Aria, D.M., 1994. Thermal-infrared remote sensing and Kirchhoff's law 1. Laboratory measurements. J. Geophys. Res. 99B (11):897–11911. https://doi.org/10.1029/93JB03600.

Schmitt, A.K., Vazquez, J., 2006. Alteration and remelting of nascent oceanic crust during continental rupture: evidence from zircon geochemistry of rhyolites and xenoliths from the Salton Trough, California. Earth Planet. Sci. Lett. 252 (3–4):260–274. https://doi.org/10.1016/j.epsl.2006.09.041.

Schmitt, A.K., Martín, A., Stockli, D.F., Farley, K.A., Lovera, O.M., 2013. (U-Th)/He zircon and archaeological ages for a late prehistoric eruption in the Salton Trough (California, USA). Geology 41 (1):7–10. https://doi.org/10.1130/G33634.1.

Shale, C.C., 1974. Ammonia injection: a route to clean stacks. Pollution Control and Energy Needs. Adv. Chem 127:pp. 195–205. https://doi.org/10.1021/ba-1973-0127.ch017 (Ch. 17).

Sobkowiak, M., Painter, P., 1995. A comparison of Drift and KBr pellet methodologies for the quantitative analysis of functional groups in coal by infrared spectroscopy. Energy Fuel 9:359–363. https://doi.org/10.1021/ef00050a022.

Spencer, R.J., 2000. Sulfate minerals in evaporate deposits. In: Alpers, C.N., Jambor, J.L., Nordstrom, D.K. (Eds.), Sulfate Mineralogy — Crystallography, Geochemistry and Environmental Science. Reviews in Mineralogy and Geochemistry 40:pp. 173–192. https://doi.org/10.2138/rmg.2000.40.3.

Sturz, A., Kamps, R., Earley, P., 1992. Temporal changes in mud volcanoes, Salton Sea geothermal area. In: Kharaka, Y., Maest, A. (Eds.), Water-Rock Interactions 2. Balkema, Rotterdam, Netherlands, pp. 1363–1366.

Svensen, H., Karlsen, D., Sturz, A., Backer-Owe, K., Banks, D., Planke, S., 2007. Processes controlling water and hydrocarbon composition in seeps from the Salton Sea geothermal system, California, USA. Geology 35 (1):85–88. https://doi.org/10.1130/G23101A.1.

Svensen, H., Hammer, Ø., Mazzini, A., Onderdonk, N., Polteau, S., Planke, S., Podladchikov, Y.Y., 2009. Dynamics of hydrothermal seeps from the Salton Sea geothermal system (California, USA) constrained by temperature monitoring and time series analysis. J. Geophys. Res. 114 (B9), B09201. https://doi.org/10.1029/2008JB006247.

Tratt, D.M., Young, S.J., Lynch, D.K., Buckland, K.N., Johnson, P.D., Hall, J.L., Westberg, K.R., Polak, M.L., Kasper, B.P., Qian, J., 2011. Remotely-sensed ammonia emission from fumarolic vents associated with a hydrothermally active fault in the Salton Sea Geothermal Field, California. J. Geophys. Res. 116 (D21), D21308. https://doi.org/10.1029/2011JD016282.

Tratt, D.M., Young, S.J., Johnson, P.D., Buckland, K.N., Lynch, D.K., 2016. Multi-year study of remotely-sensed ammonia emission from fumaroles in the Salton Sea geothermal field. Proceedings, 8th IEEE Workshop on Hyperspectral Image and Signal Processing: Evolution in Remote Sensing — WHISPERS (Los Angeles, CA, August 21–24, 2016).

Van Doesburg, J.D.J., Vergouen, L., van der Plas, L., 1982. Konyaite, $Na_2Mg(SO_4)_2 \cdot 5H_2O$, a new mineral from the Great Konya Basin, Turkey. Am. Mineral. 67 (9–10), 1035–1038.

Vaughan, R.G., Hook, S.J., Calvin, W.M., Taranik, J.V., 2005. Surface mineral mapping at Steamboat Springs, Nevada, USA, with multi-wavelength thermal infrared images. Remote Sens. Environ. 99 (1–2):140–158. https://doi.org/10.1016/j.rse.2005.04.030.

Veatch, J.A., 1858. Notes of a visit to the mud volcanoes in the Colorado Desert in the month of July 1857. Am. J. Sci., 2nd Ser. 26, 288–295.

Veatch, J., 1860. Salses or mud volcanoes of the Colorado Desert. Hesperian 3 (5), 481–489.

Warren, D.W., Boucher, R.H., Gutierrez, D.J., Keim, E.R., Sivjee, M.G., 2010. MAKO: a high-performance, airborne imaging spectrometer for the long-wave infrared. Proc. SPIE 7812:78120N. https://doi.org/10.1117/12.861374.

Young, S.J., Johnson, B.R., Hackwell, J.A., 2002. An in-scene method for atmospheric compensation of thermal hyperspectral data. J. Geophys. Res. 107 (D24):4774. https://doi.org/10.1029/2001JD001266.

Younker, L.W., Kasameyer, P.W., Tewhey, J.D., 1982. Geological, geophysical, and thermal characteristics of the Salton Sea geothermal field, California. J. Volcanol. Geotherm. Res. 12 (3–4):221–258. https://doi.org/10.1016/0377-0273(82)90028-2.